Journal of Catalysis 275 (2010) 45–60

Contents lists available at ScienceDirect

Journal of Catalysis

journal homepage: www.elsevier.com/locate/jcat

Correlation of structural characteristics with catalytic performance of $CuO/Ce_xZr_{1-x}O_2$ catalysts for NO reduction by CO

Lianjun Liu [a], Zhijian Yao [a], Bin Liu [a], Lin Dong [a,b,*]

[a] Key Laboratory of Mesoscopic Chemistry of MOE, School of Chemistry and Chemical Engineering, Nanjing University, Nanjing 210093, PR China
[b] Modern Analysis Center, Nanjing University, Nanjing 210093, PR China

ARTICLE INFO

Article history:
Received 28 April 2010
Revised 12 July 2010
Accepted 13 July 2010

Keywords:
$Ce_xZr_{1-x}O_2$
Structure
Interaction
Adsorption
NO reduction

ABSTRACT

NO reduction by CO reaction was studied over a series of $CuO/Ce_xZr_{1-x}O_2$ catalysts with different copper loadings and Ce/Zr molar ratios to evaluate the correlation of their structural characteristics with catalytic performance. These catalysts were investigated in detail by means of thermogravimetric analysis (TGA/DSC), X-ray diffraction (XRD), Raman spectroscopy, high-resolution transmission electron microscopy (HR-TEM), electron paramagnetic resonance (EPR), UV–vis spectroscopy, X-ray photoelectron spectroscopy (XPS) and H_2-temperature-programmed reduction (H_2-TPR) and in situ Fourier transform infrared spectroscopy (FTIR). The results demonstrated that the ceria-rich (pseudocubic t'') phase could disperse and stabilize the copper species more effectively and resulted in stronger interaction with copper than the zirconia-rich (t) phase. Furthermore, compared with the zirconia-rich phase, the synergistic interaction of copper with ceria-rich phase easily promoted the reduction of copper species and support surface oxygen, as well as the activation of adsorbed NO species. Therefore, $CuO/Ce_{0.8}Zr_{0.2}O_2$ catalyst exhibited the higher activity for NO reduction than $CuO/Ce_{0.5}Zr_{0.5}O_2$ and $CuO/Ce_{0.2}Zr_{0.8}O_2$. A surface model was proposed to discuss these catalytic properties. The copper species at the interfacial area did not maintain an epitaxial relationship with $Ce_xZr_{1-x}O_2$, while could penetrate into the $Ce_xZr_{1-x}O_2$ surface lattice by occupying the vacant site on the exposed (1 1 1) plane. The type and coordination environment of copper species were different in ceria-rich and zirconia-rich phases surface, and their stabilities were related to the lattice strains.

1. Introduction

Substitutional ceria–zirconia solid solutions have attracted much interest in recent years because of their extensive use in a number of different fields, for example, as active supports or "oxygen buffers" in three-way catalysis elimination of CO, NO_x and hydrocarbons. Their crystal structures and local order are therefore widely investigated by either theoretical calculation or XRD, Raman, neutron spectroscopy, extended X-ray absorption fine structure (EXAFS) and HR-TEM [1–8]. Until now, five different phases are identified depending on the cerium content: one monoclinic phase (m, < 5%, $P2_1/c$), three tetragonal phases (t, t', t'', 15% < x < 90%, $P4_2/nmc$) and one cubic phase (c, > 90%, $Fm3m$) [5]. The physicochemical properties of these solids are also intensively studied. Along with the influence of preparation method and complex composition (chemical homogeneity) [9–11], the structural and textural properties (thermal stability, surface area, crystallite size) [12,13], oxygen storage capacity [14–17], redox and adsorption behaviors (CH_3OH, CO, NO, NO_2) [18–21], and dynamics of oxygen storage [22], as well as catalytic activity [23,24], are checked. The focus has been on examining the possible correlation of structural features with these properties. Results seem to indicate that $Ce_xZr_{1-x}O_2$ ($0.5 < x < 0.8$) solid solution has a superior performance in terms of overall reduction and total oxygen storage. This behavior is consistent with a structural modification of the fluorite cell induced by the introduction of zirconia, which brings out a higher lability in surface and bulk oxygen ions, thus enhancing their diffusion rate [22].

Other than this, in addition to noble metals (Rh, Pt, Pd, Au) supported on ceria–zirconia-related catalysts [25–30], considerable efforts have been devoted to develop the promising copper-based catalyst [31–41] for preferential oxidation of CO and selective reduction of NO. Typically, these reports pay close attention to the influence of particle size, metal–support interaction and active species on the catalytic activity, in order to improve the intrinsic performance and understand the reaction mechanism. It has been agreed that the well-known enhancement of the total oxidation activity of $CuO–CeO_2$ is attributed to the "synergistic" effect. Skårman et al. [35a] have attributed this to an epitaxial

* Corresponding author at: Key Laboratory of Mesoscopic Chemistry of MOE, School of Chemistry and Chemical Engineering, Nanjing University, Nanjing 210093, PR China. Fax: +86 25 83317761.
E-mail address: donglin@nju.edu.cn (L. Dong).

0021-9517/$ - see front matter © 2010 Elsevier Inc. All rights reserved.
doi:10.1016/j.jcat.2010.07.024

copper phase on top of the fluorite type CeO_2. Although a large amount of structural and electronic studies on the $CuO–CeZrO_2$ system are carried out, the interaction of copper species with the predominately exposed plane of ceria–zirconia has been frequently dismissed. It is still important to emphasize that the analysis of the dispersion behaviors and structural characteristics of copper species on the surface of metastable *t* (zirconia-rich), *t′* and *t″* (ceria-rich) phases cannot be ruled out, especially the influence on the catalytic properties for NO reduction. These issues remain ambiguous that needs a better understanding at the atomic level.

Previously, we studied the coordination states and reduction properties of $CuO/WO_3/CeO_2$, CuO/Fe_2O_3 and $CuO/t–ZrO_2$ catalysts [42,43]. On this basis, the present work fundamentally approached the structural characteristic, dispersion, reduction, adsorption/desorption behaviors and activity of the representative $CuO/Ce_xZr_{1-x}O_2$ catalysts with varying the copper loadings and Ce/Zr molar ratios, which were characterized by TGA/DSC, XRD, Raman, HR-TEM, UV–vis, EPR, XPS, H_2-TPR and in situ FTIR. The good NO + CO model reaction was also performed. The aim was to establish the composition–structure–property relationships, which would be beneficial for the design and rationalization of the practical catalysts.

2. Experimental

2.1. Catalyst preparation

$Ce_xZr_{1-x}O_2$ ($x = 0.2$, 0.5, 0.8) oxides were prepared by the co-precipitation method [41]. In brief, a requisite amount of $(NH_4)_2Ce(NO_3)_6{\cdot}6H_2O$ and $Zr(NO_3)_4{\cdot}5H_2O$ were dissolved in distilled water, and the excess ammonia (25%) was slowly dropped to the mixture solution with vigorously stirring until pH = 10. The resulting solution was kept in stirring for another 3 h, aged overnight and then filtered, washed with distilled water until no pH change. The obtained solids were first dried at 110 °C overnight, and then calcined at 500 °C in the flowing air for 4 h. The $CuO/Ce_xZr_{1-x}O_2$ catalysts were prepared by incipient wetness impregnation method with the solution containing $Cu(NO_3)_2$. The CuO loading amount was 0.3, 0.6, 0.9, 1.2, 1.5 mmol/100 m^2 $Ce_xZr_{1-x}O_2$. The mixture was kept stirring for 3 h and was evaporated at 100 °C. The resultant materials were calcined at 450 °C in the flowing air for 4 h. For simplification, these catalysts were denoted as yCu/C_2Z_8, C_5Z_5, C_8Z_2, where y was the copper loading amount.

2.2. Catalyst characterization

The specific surface areas of these supports were determined via nitrogen adsorption at 77 K (Micromeritics ASAP-2020) with the Brunauer–Emmett–Teller (BET) method.

The change in the weight of the uncalcined supports was monitored by thermogravimetric analysis (TGA) in the flowing air from room temperature to 900 C. A commercial Netzsch TGA/DSC analyzer (ATA 449C-Thernak Star 300) was employed for this purpose.

XRD patterns were recorded on a Philips X'pert Pro diffractometer using Ni-filtered Cu Kα radiation ($\lambda = 0.15418$ nm). The X-ray tube was operated at 40 kV and 40 mA. The mean grain sizes (D_β) from the (1 1 1) plane and strain (ε) of these samples were calculated by the Scherrer equation ($D_\beta = K\lambda/\beta\cos\theta$) and $\varepsilon = \beta/4tg\theta$, respectively.

Raman spectra were collected on a Jobin–Yvon (France–Japan) T64000 type Laser Raman spectroscopy using Ar^+ laser beam, operating with an excitation wavelength of 516 nm and the laser power of 300 mW.

HR-TEM images of these samples were obtained by a JEM-2100CX system. The six samples were dispersed in ethanol and kept in an ultrasonic bath for 15 min, then deposited on a carbon-covered copper grid for measurement.

UV–vis DRS spectra were recorded in the range of 200–900 nm by a UV–vis–NIR 5000 spectrophotometer. $BaSO_4$ was used as the reference for baseline emendation.

EPR measurements were performed on a Bruker EMX-10/12 spectrometer operating at X-band frequency ($\nu \approx 9.4$ GHz) and 100-kHz filed modulation. The spectra of these catalysts were recorded at 77 K.

XPS analysis was performed on a Thermo ESCALAB 250 high performance electron spectrometer, using Al Kα radiation (1486.6 eV) operating at an accelerating power of 150 W. All binding energies (BE) were referenced to the adventitious C 1s at 284.6 eV. This reference gave BE values with an accuracy at ±0.1 eV. Charge effects were corrected by adjusting the Ce $3d_{3/2}$ peak (*u‴*) to a position of 917.0 eV.

H_2-TPR was carried out in a quartz U-tube reactor connected to a thermal conduction detector with H_2–Ar mixture (7.0% H_2 by volume) as reductant. Before switched to the H_2–Ar stream, the sample (50 mg) was pretreated in a N_2 stream at 100 °C for 1 h. After that, TPR started from room temperature to 650 °C at a rate of 10 °C min^{-1}.

In situ FTIR spectra were collected from 400 to 4000 cm^{-1} at a resolution 4 cm^{-1} (number of scans, ~32) on a Nicolet 5700FTIR spectrometer. The catalysts (about 25 mg) were mounted in an IR cell and pretreated for 1 h at 100 °C in the flowing N_2 atmosphere. After cooling to room temperature, the self-supporting wafer were exposed to a controlled stream of CO–Ar (10% CO) or/and NO–Ar (5% NO) at a rate of 5.0 ml min^{-1} for 30 min. In situ FTIR spectra (temperature-programmed reduction and reaction) were recorded at various target temperatures (at every 25 °C) by subtraction of the background reference (collected from the gas data at each temperature without the samples).

2.3. Catalytic activity tests

The activities of the catalysts were determined under light-off procedure, involving a feed steam with a fixed composition, 5% NO, 10% CO and 85% He by volume as diluents. The catalysts (50 mg) were pretreated in N_2 stream at 100 °C for 1 h and then cooled to room temperature, after that, the mixed gases were switched on. The reactions were carried out at different temperatures with a space velocity of 12,000 mL g^{-1} h^{-1}. Two gas chromatographs equipped with thermal conduction detections were used for analyzing the production. Column A with Paropak Q for separating N_2O and CO_2 and column B packed with 5A and 13X molecule sieve (40–60 M) for separating N_2, NO and CO. Kinetic measurements were performed under differential reaction conditions, with ~15 mg catalyst to limit the conversion between 5% and 40%. The turnover frequency (TOF, s^{-1}) of NO over per copper atom was calculated by this equation, i.e., $TOF = P \cdot V_s \cdot C \cdot V_{NO}\% \times 10^{-6}/R \cdot T \cdot n_{Cu}$ (V_s = space velocity, C = NO conversion, $V_{NO}\%$ = NO concentration, n_{Cu} = molar ratio of copper species). The content of surface copper species was determined by XPS.

3. Results and discussion

3.1. Structural characterization (TGA, XRD, Raman, HR-TEM)

3.1.1. TGA and XRD analysis

The TGA/DSC analysis of these supports before calcination provided some information on the interaction between cerium and zirconium hydrate with different molar ratios. As shown in Fig. 1, these endothermic peaks of the three samples in the range 70–300 °C were primarily due to the loss of nondissociative

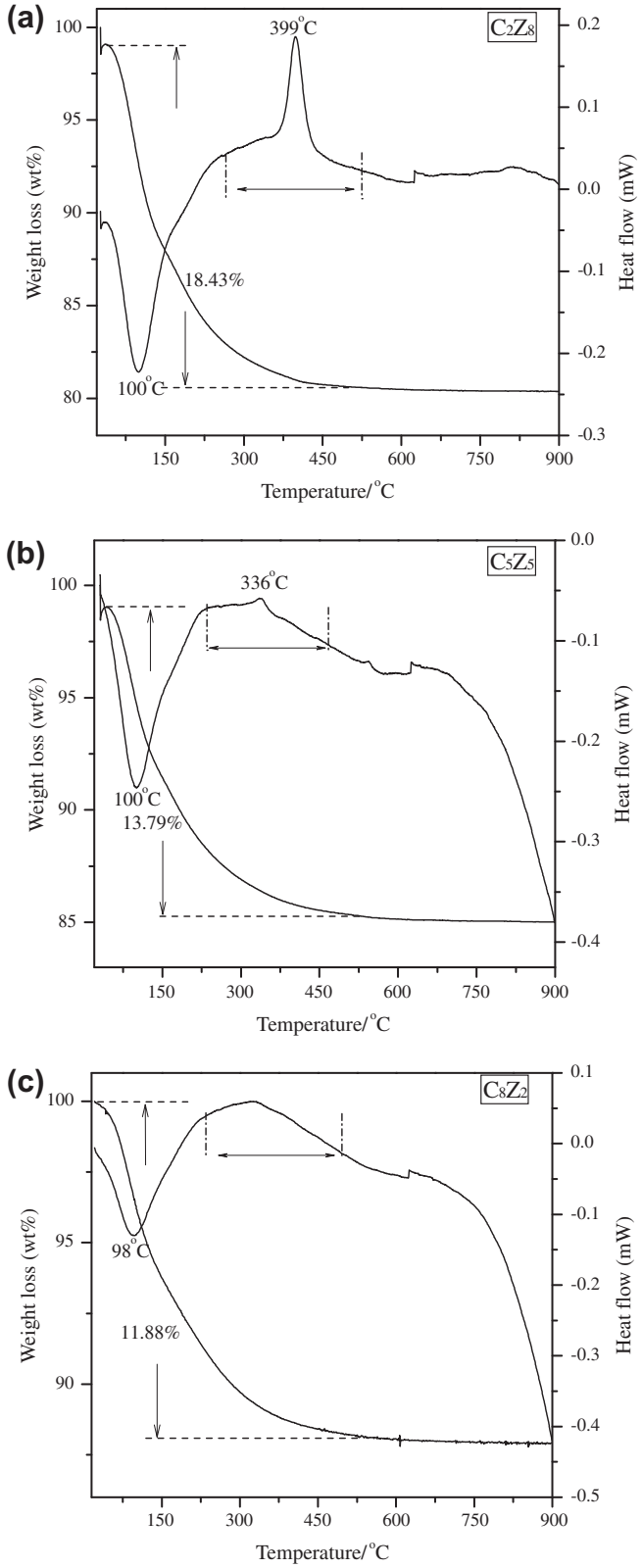

Fig. 1. TG–DSC curves of these ceria–zirconia supports (a) C_2Z_8, (b) C_5Z_5, and (c) C_8Z_2.

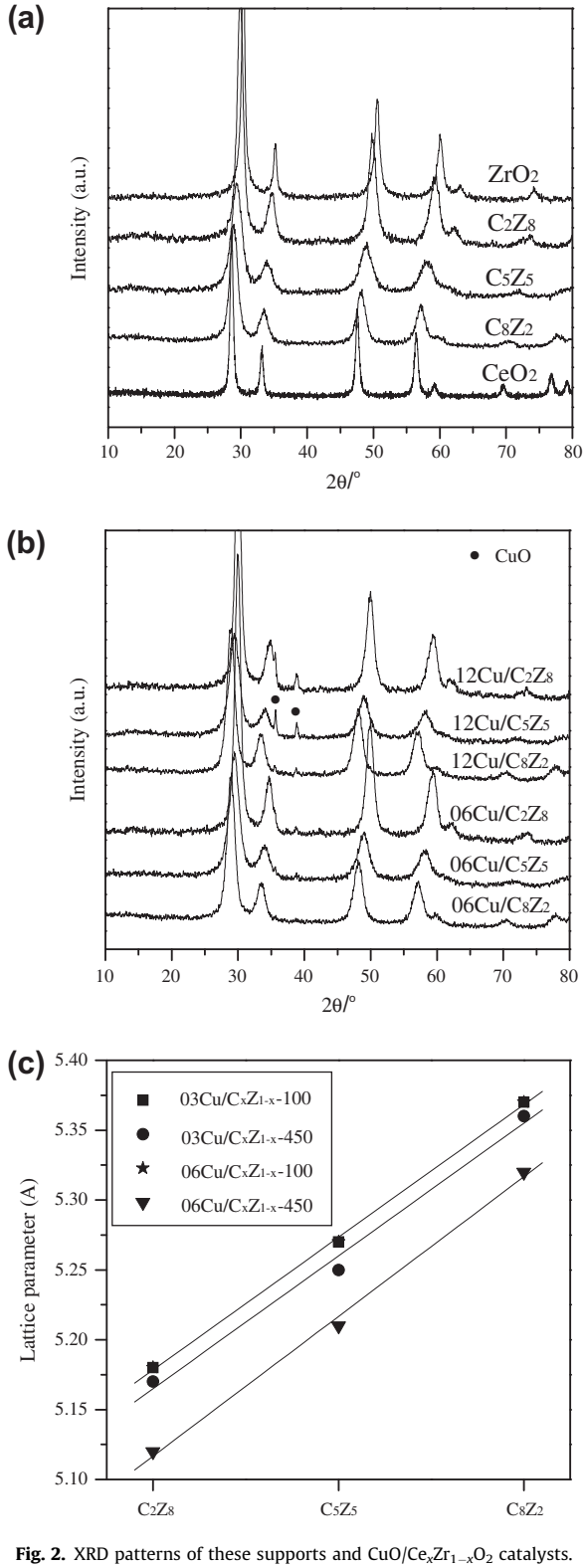

Fig. 2. XRD patterns of these supports and $CuO/Ce_xZr_{1-x}O_2$ catalysts.

adsorbed water and the hydroxyl groups [6]. These second exothermic peaks at higher temperatures (C_2Z_8: 399 °C, C_5Z_5: 336 °C) were related to the heat effect on the phase transformation from amorphous to tetragonal crystallites, and the broad peak in C_8Z_2 should be associated with the crystallization of cubic phase. Moreover, the weight loss of the samples was from ambient up to 500 °C. Apparently, the amorphous to crystalline transition of $Ce_xZr_{1-x}O_2$ was affected by the sample compositions [11], since the transition temperatures and weight loss increased as the cerium content decreased.

When compared with cubic ceria and tetragonal zirconia patterns (Fig. 2a), the diffraction peaks of the mixed oxides were

Table 1
The surface area, grain size, lattice parameter, strain and space group of $Ce_xZr_{1-x}O_2$ and $06Cu/Ce_xZr_{1-x}O_2$ catalysts.

Samples	BET (m^2/g)	Grain size (nm)	Lattice parameter (Å)	Lattice strain (%)	Space group
ZrO_2	56.9	16.4	5.09	0.46	*t*, $P4_2/nmc$
CeO_2	27.0	14.4	5.40	0.55	*c*, $Fm3m$
C_2Z_8	63.1	7.7	5.18	0.99	*t*, $P4_2/nmc$
C_5Z_5	56.6	5.3	5.27	1.44	*t″*, $P4_2/nmc$
C_8Z_2	48.8	5.7	5.37	1.42	*t″*, $P4_2/nmc$
$06Cu/C_2Z_8$	–	9.9	5.12	0.76	*t*, $P4_2/nmc$
$06Cu/C_5Z_5$	–	6.8	5.21	1.13	*t″*, $P4_2/nmc$
$06Cu/C_8Z_2$	–	6.5	5.32	1.21	*t″*, $P4_2/nmc$

broadened due to the small crystalline size [3] and shifted to high angles as a function of zirconium content, indicating the phase transition from the cubic fluorite structure to the tetragonal structure [5]. The symmetrical peaks of $Ce_xZr_{1-x}O_2$ suggested the formation of single ceria–zirconia solid solution (no peak splitting for the presence of two phases) [12a]. However, it was difficult to explore the intermediate tetragonal (*t′*, *t″*) phase at high zirconium content due to the limitation of XRD. As shown in Fig. 2b, after the impregnation of copper species with low loading, very weak peaks for crystalline CuO appeared in $06Cu/C_2Z_8$ and $06Cu/C_5Z_5$ but were absent in $06Cu/C_8Z_2$. When at high loading, the diffraction intensity of crystalline CuO increased distinguishingly in $12Cu/C_2Z_8$ and

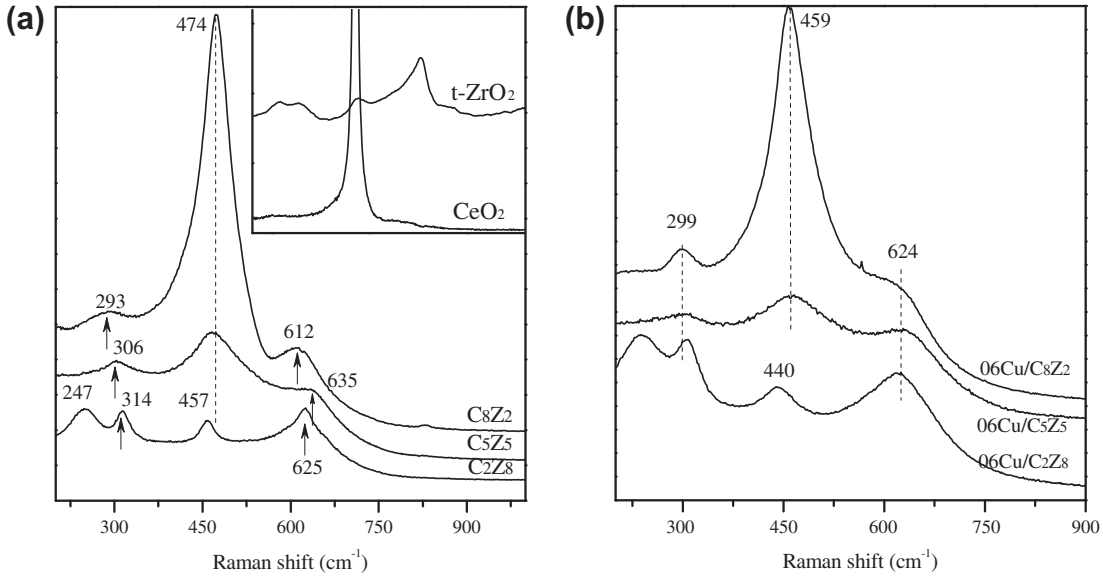

Fig. 3. Raman spectra of these supports and $06Cu/Ce_xZr_{1-x}O_2$ catalysts.

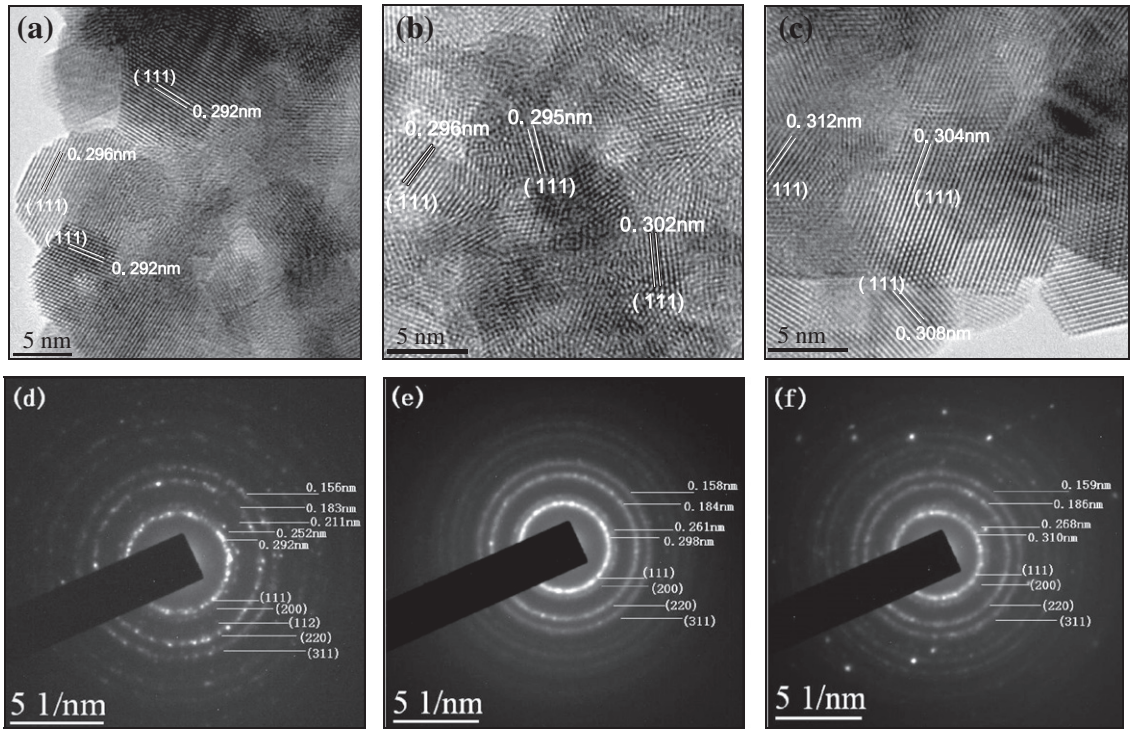

Fig. 4. HR-TEM and selected area electron diffraction (SAED) images of these $06Cu/Ce_xZr_{1-x}O_2$ catalysts (a and d) $06Cu/C_2Z_8$, (b and e) $06Cu/C_5Z_5$, and (c and f) $06Cu/C_8Z_2$.

12Cu/C_5Z_5, while was very weak in 12Cu/C_8Z_2. These results indicated the difference in their dispersion capacity (details seen in Fig. S1), and the ceria-rich support seemed to disperse and anchor the copper species more effectively than the zirconia-rich one.

The grain size, lattice parameter and strain of the mixed oxides before and after copper impregnation are summarized in Table 1. The data shows that the grain size of C_2Z_8 is bigger than that of C_8Z_2 and C_5Z_5, and all of them slightly increase after the introduction of copper species. Table 1 also shows that the lattice parameters of cubic CeO_2 and tetragonal ZrO_2 are 5.40, 5.09 Å, respectively. When $x = 0.8$, 0.5, 0.2, the lattice parameters of $Ce_xZr_{1-x}O_2$ decrease from 5.37, 5.27 to 5.18 Å, respectively. This observation is due to the displacement of Ce^{4+} ions ($r^{4+}_{Ce} = 0.97$ Å) by the smaller zirconium ions ($r^{4+}_{Zr} = 0.84$ Å) [9–12]. Interestingly, Fig. 2c showed that the lattice parameter of ceria–zirconia did not change after the addition of copper species without calcination. However, calcination at 450 °C led to the lattice contraction, probably due to the incorporation of monolayer copper ($r^{2+}_{Cu} = 0.73$ Å) into ceria–zirconia surface/subsurface layers. Nevertheless, the copper did not insert into the bulk lattice to form a new $CuCeZrO_x$ solid solution, because ceria–zirconia still maintained their original crystal structures with no additional Bragg-position shift (Fig. S2). Apart from this, the introduction of Zr species led to extra force that increased the lattice strain of CeO_2. The ceria-rich support exhibited the relatively high lattice strain, while the zirconia-rich displayed the low level. As reported previously [2,17], strain was a measurement of the lattice stress existing in the materials because of surface effects and/or the crystal imperfections. Accordingly, the above difference in strains should be related to the large density of oxygen defects in C_8Z_2 and small in C_2Z_8, which might be caused by the defective pseudocubic (t'') structure of C_8Z_2 and nondefective tetragonal structure of C_2Z_8 [17]. In addition, the impregnation of copper species slightly reduced the lattice strains of C_8Z_2, C_5Z_5 and C_2Z_8. The strains of the resultant catalysts were in the order of 06Cu/C_8Z_2 > 06Cu/C_5Z_5 > 06Cu/C_2Z_8. Therefore, these stabilized copper species could interact with the underlying supports, and the interaction between them was 06Cu/C_8Z_2 > 06Cu/C_5Z_5 > 06Cu/C_2Z_8 in sequence.

3.1.2. Raman spectra analysis

The XRD results were well complemented by Raman spectra. As shown in Fig. 3a, C_2Z_8 maintained the tetragonal structure (identical to t-ZrO_2) [3,5]. C_5Z_5 showed one weak band at ca. 474 cm^{-1}, which was due to the characteristic F_{2g} Raman active mode of the fluorite type lattice [9,12]. Two weak bands at ca. 306 and 635 cm^{-1} were attributed to the tetragonal substitution of oxygen atoms from their ideal fluorite lattice position and the nondegenerate Longitudinal Optical (LO) mode of ceria (linked to oxygen vacancies in the ceria lattice), respectively [6,9,12]. Compared with pure CeO_2, C_8Z_2 displayed the broad F_{2g} band, which was related to either the small size or the formation of oxygen vacancy [6,30].

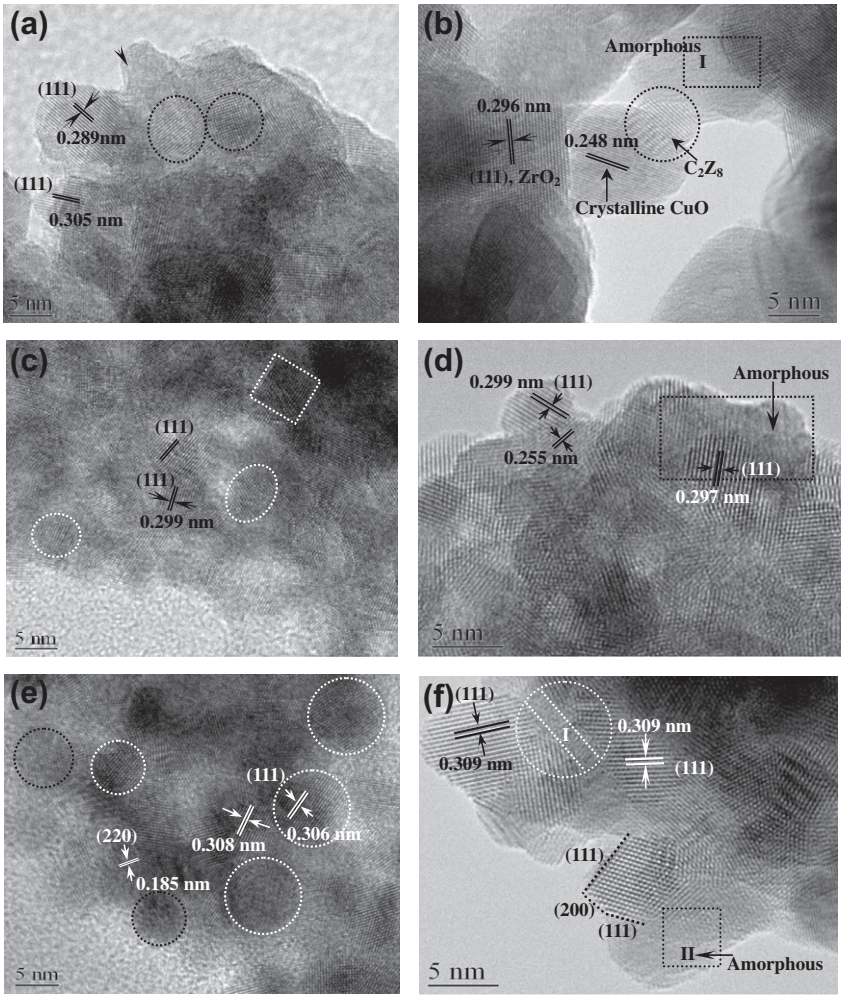

Fig. 5. HR-TEM images of these 06Cu/$Ce_xZr_{1-x}O_2$ catalysts dried at 100 °C and calcined at 450 °C, respectively, (a and b) 06Cu/C_2Z_8, (c and d) 06Cu/C_5Z_5, and (e and f) 06Cu/C_8Z_2.

Additionally, Raman bands at 306 and 635 cm^{-1} red shifted to 293 and 612 cm^{-1} with changing C_5Z_5 to C_8Z_2. This shift is associated with more Zr ions in C_5Z_5 and accompanied by *t* phase-like lattice distortions [5]. The above observations also predicted the possibility of the existence of metastable *t″* phase or/and the association with *t* phase-like lattice distortion in the C_5Z_5 and C_8Z_2 systems [5,17]. A comparison of the data from TGA/DSC, XRD and Raman showed that the tetragonal (*t*) phase was predominant in C_2Z_8; pseoducubic (*t″*) phase was predominant in C_8Z_2 and C_5Z_5. In fact, the *t″* phase differed from the *c* phase only in that some oxygen ions were displaced from their ideal fluorite positions to new tetragonal positions, while all cations remained in their fcc positions [5]. Although C_8Z_2 and C_5Z_5 were in the same pseoducubic (*t″*) phase, C_8Z_2 preferentially exhibited the cubic characteristic, while C_5Z_5 mainly showed the tetragonality. This was in agreement with the report that the tetragonality of three tetragonal phases (t, t'', t'') increased with zirconia content [14]. As shown in Fig. 3b, further evidence of copper incorporation into the surface/subsurface position of $Ce_xZr_{1-x}O_2$ was given by the red shift (from 474 to 459 and 457 to 440 cm^{-1}) and width observed in the F_{2g} peaks. Since the grain size of $CuO/Ce_xZr_{1-x}O_2$ increased, these observations certainly presented the influences of the interaction between copper species and ceria–zirconia and their inhomogeneous strains.

3.1.3. HR-TEM analysis

HR-TEM was performed to ascertain the crystallite growth and morphology of the three representative catalysts. For $06Cu/C_2Z_8$ at high magnifications (Fig. 4a), it contained the smoothly interfaced particles (~6–10 nm) with the irregular shapes. Only one kind of

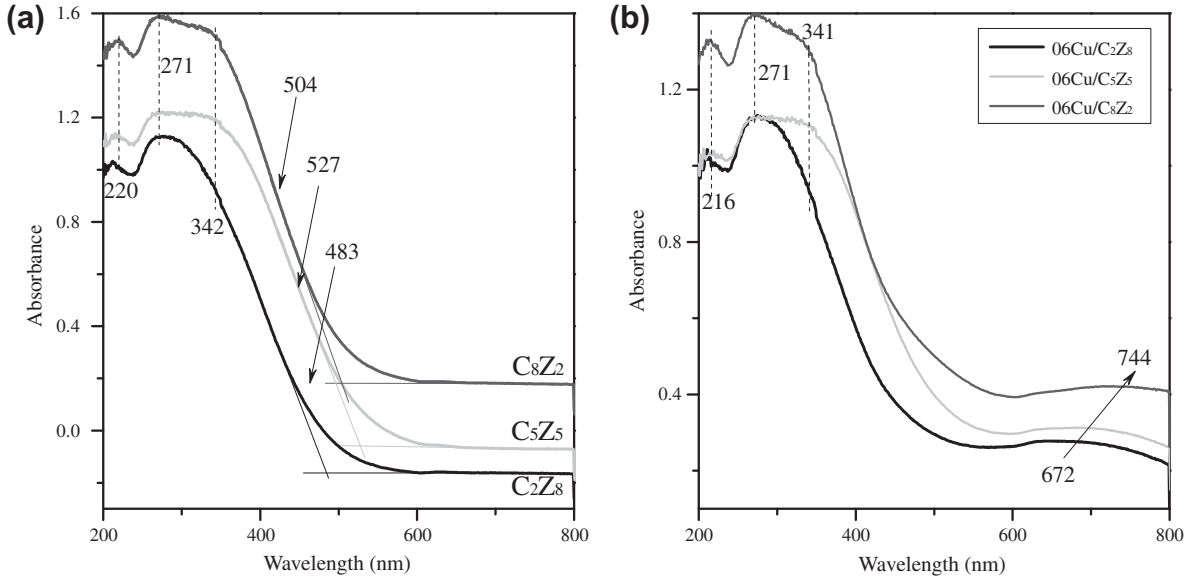

Fig. 6. UV–vis spectra of (a) these supports and (b) $06Cu/Ce_xZr_{1-x}O_2$ catalysts.

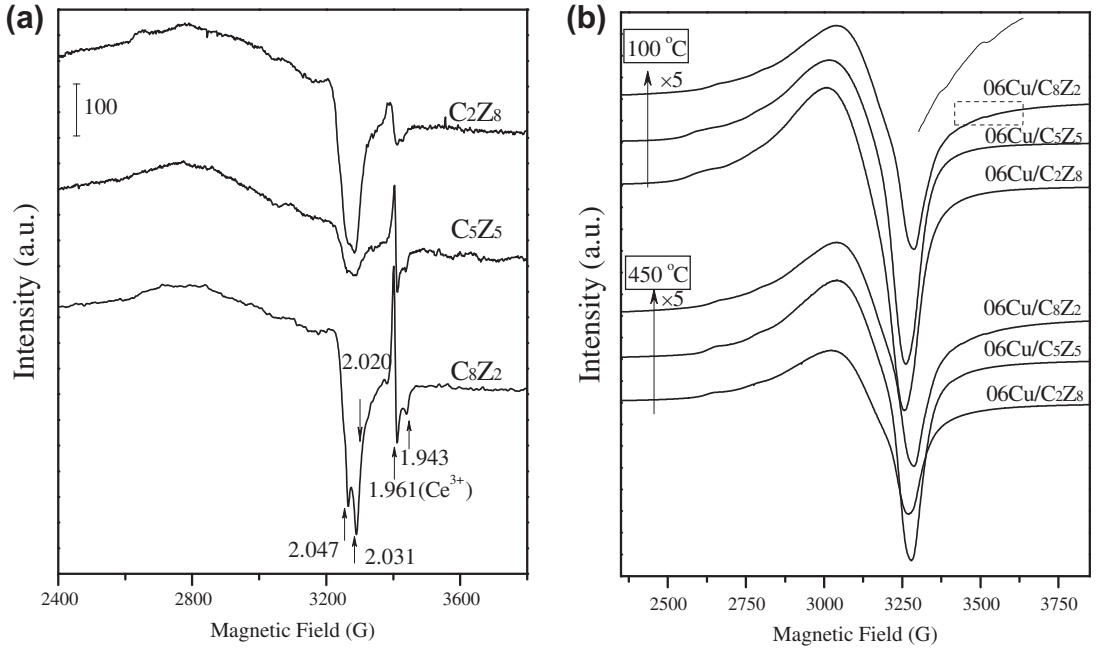

Fig. 7. EPR spectra of (a) $Ce_xZr_{1-x}O_2$ and (b) $06Cu/Ce_xZr_{1-x}O_2$ catalysts dried at 100 °C and calcined at 450 °C, respectively.

periodicity of lattice fringes (~0.292 nm) can be observed, which was compatible with the distance expected between the (1 1 1) reticular plane of C_2Z_8. The results indicated that the most frequently exposed crystal plane of C_2Z_8 should be (1 1 1) plane. Judging from the continuous rings in the selected area diffraction (SAD) pattern (Fig. 4d), there was an evidence for the presence of the tetragonal phase, viewed in the (1 1 2) facet with the spacing of 0.211 nm [6]. For $06Cu/C_5Z_5$ sample (Fig. 4b), the high presence of Moiré fringes was taken as an interaction of aggregates composed of epitaxially interfaced nanocrystallites, and it was also en-

Table 2
EPR spin Hamiltonian parameters.

Samples	Temperature (°C)	Assignment	$g_{\parallel}$	$g_{\perp}$	$A_{\parallel}$(Cu) (G)
C_2Z_8	500	Ce^{3+}	1.961	1.943	–
C_5Z_5		Ce^{4+}–O_2^{-}	2.031	2.020	–
C_8Z_2		Ce^{3+} and oxygen vacancy	g = 2.047		–
$06Cu/C_2Z_8$	100	Isolated surface Cu^{2+}	2.318	2.055	179
		Interacting Cu^{2+}	2.128	2.128	Not resolved
	450	Isolated surface Cu^{2+} in the tetragonal vacant site	2.329	2.044	140
		Interacting Cu^{2+}	2.122	2.122	Not resolved
$06Cu/C_5Z_5$	100	Isolated surface Cu^{2+}	2.302	2.051	199
		Interacting Cu^{2+}	2.114	2.114	Not resolved
	450	Isolated surface Cu^{2+}	2.329	2.039	140
			2.106	2.106	Not resolved
$06Cu/C_8Z_2$	100	Isolated surface Cu^{2+}	2.330	2.045	125
		Interacting Cu^{2+}	2.113	2.113	Not resolved
	450	Isolated surface Cu^{2+} in the cubic vacant site	2.335	2.038	132
		Interacting Cu^{2+}	2.110	2.110	Not resolved

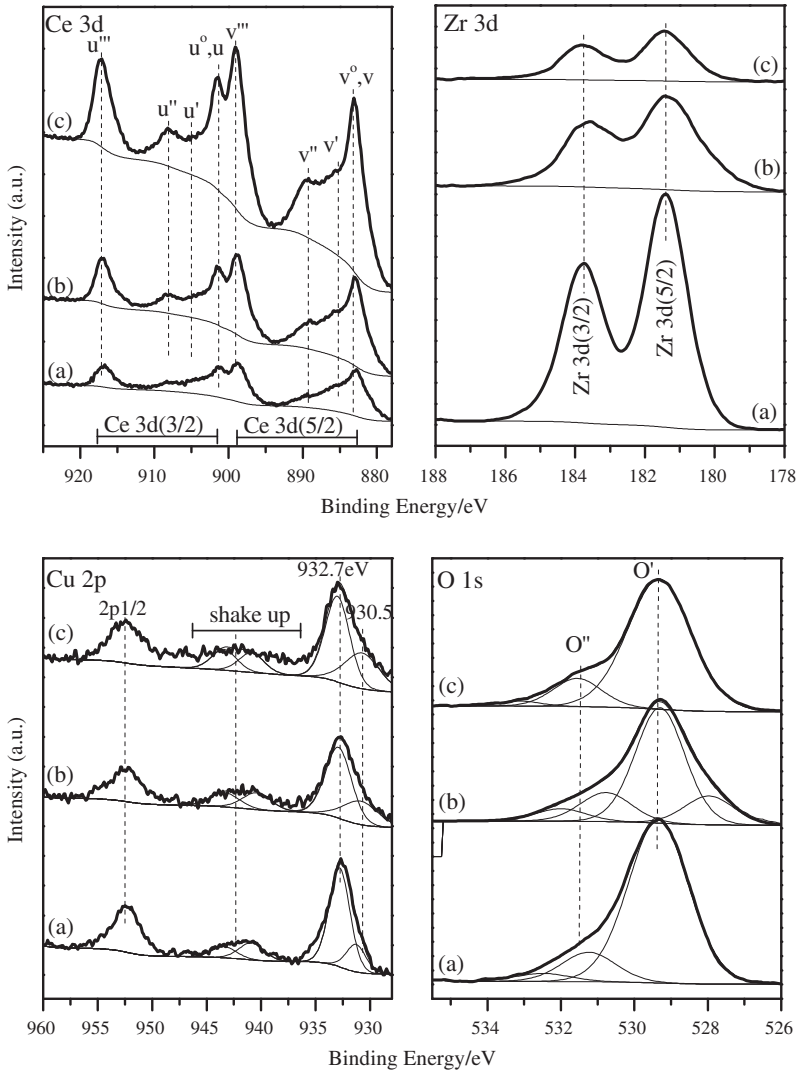

Fig. 8. XPS spectra (Ce 3d, Zr 3d, Cu 2p, O 1s) of these $06Cu/Ce_xZr_{1-x}O_2$ catalysts.

closed by the (1 1 1) plane with the interplanar spacing of 0.296 nm. The patterns of the majority of nanocrystal imaged in the SAD (Fig. 4e) could again be indexed to the fluorite structure (metastable pseudocubic and tetragonal without monoclinic trace). For 06Cu/C_8Z_2 sample (Fig. 4c and f), the image (number of block-shaped particles, ~5–8 nm) clearly displayed the (1 1 1) lattice fringes with interplanar spacing of 0.308 nm, and some extended defects such as dislocations, grain boundaries and staking faults observed inside particles. From the SAD pattern, the pseudocubic structure could be identified [7,11]. Therefore, the above-mentioned analysis reasonably revealed that $Ce_xZr_{1-x}O_2$ oxides were shown to predominantly expose the (1 1 1) plane. The crystal phases and space groups of these solid oxides were summarized in Table 1.

HR-TEM was further performed on the fresh and calcined 06Cu/$Ce_xZr_{1-x}O_2$ samples to obtain fine structural details of the nano-sized particles when dispersed onto supports. Fig. 5a shows a HR-TEM image of 06Cu/C_2Z_8 before calcination, which contains the aggregated particles with the average size ~7 nm. The spacing of these lattice fringes is around 0.289 nm, which is ascribed to the (1 1 1) crystallographic planes of C_2Z_8 support. However, no crystal planes of copper can be seen in the lattice-fringe image. After calcined at 450 °C (Fig. 5b), a few CuO crystallites appear with the lattice spacing 0.248 nm, but not frequently enough to account for all impregnated copper and without any obvious epitaxial relationship to C_2Z_8 support. Crystallographic planes at 0.296 nm corresponding to (1 1 1) planes of C_2Z_8 support are not parallel to planes at 0.248 nm due to (1 1 1) plane of CuO [35b]. In addition, apparently amorphous surface CuO_x clusters are found evenly distributed on top of or at the edge of zirconia crystal. Similar phenomena could also be observed in 06Cu/C_5Z_5 sample (Fig. 5c and d). In comparison with 06Cu/C_8Z_2 before and after calcination (Fig. 5e and f), HR-TEM images provide obvious evidence that the original spherical-shaped particles (5–7 nm) disappear, while block-shaped particles exhibit sharp edges and distinct flat surface presenting a higher crystallinity factors. Interestingly, the C_8Z_2 particle size distribution has not been broadened with respect to the fresh one. The frequently exposed plane is also the (1 1 1) facet with the lattice spacing of 0.308 nm. Both these electron diffraction results and lack of detection of distinct copper crystals in the HR-TEM images suggest a high dispersion of copper phase. Moreover, in the zone of I and II, it is seen that the amorphous copper seem to be embedded in the lattice of C_8Z_2 support. These results reveal that (1) copper oxide and ceria–zirconia unlikely maintain an epitaxial relationship due to the mismatch between crystal lattices of CuO and the supports. Skårman et al. [35a] also proposed that tenorite oxides, where all Cu was in the +2 state, imposed a strong monoclinic distortion of the unit cell and would break loose from the CeO_2 film support. (2) Compared with the zirconia-rich phase, a stronger interaction between copper species and ceria-rich phase induces the change of its morphology. (3) Copper in small amounts (lower than the dispersion capacity) has a strong tendency to associate with ceria-rich phase, and excess copper (higher than the dispersion capacity) forms bulk CuO particles on the zirconia-rich surface. This supports the XRD results.

3.2. Chemical and electronic states of CuO/$Ce_xZr_{1-x}O_2$ catalysts (UV, EPR, XPS)

3.2.1. UV–vis and EPR analysis

The information on the surface electronic states can be obtained from UV–vis diffuse reflectance measurements. As shown in

Table 3
XPS elementary surface concentration of 06Cu/$Ce_xZr_{1-x}O_2$ catalysts.

Samples	Atomic concentration				Atomic ratios		
	Ce (at.%)	Zr (at.%)	Cu (at.%)	O (at.%)	Ce/Zr	Cu/(Ce + Zr)	O/(Ce + Zr + Cu)
06Cu/C_2Z_8	5.3	16.7	2.9	60.0	0.32 (0.25)	0.13	2.41
06Cu/C_5Z_5	12.0	10.1	3.7	55.5	1.18 (1.0)	0.16	2.15
06Cu/C_8Z_2	20.4	4.1	4.0	52.1	4.97 (4.0)	0.16	1.83

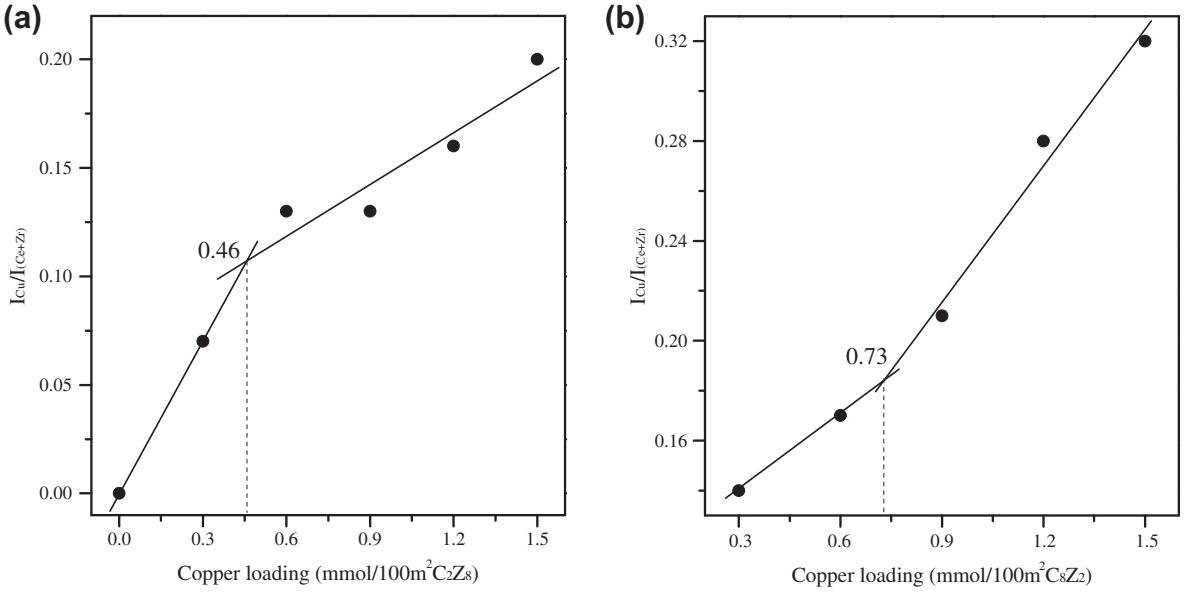

Fig. 9. XPS peak intensity ratio $I_{Cu}/I_{(Ce+Zr)}$ versus the content of copper oxide in Cu/C_2Z_8 and Cu/C_8Z_2 samples.

Fig. 6a, two bands for C_5Z_5 and C_8Z_2 supports at ca. 271 and 342 nm can be attributed to $O^{2-} \rightarrow Ce^{4+}$ charge transfer and interband transitions [12a], whereas only a broad one at 271 nm appeared in C_2Z_8 sample. The absorption band at 255 nm corresponding to the $O^{2-} \rightarrow Ce^{3+}$ charge transfer transition [17] was not clearly observed. Eight-coordinated tetravalent Zr species (like those of cubic and tetragonal zirconia) were responsible for the absorption in the range 200–220 nm [44]. On the other hand, the position of absorption edges was located in 504, 527 and 483 nm for C_8Z_2, C_5Z_5 and C_2Z_8 in sequence and did not keep any direct linear relationship with the composition. This may be due to the similar particle sizes of these oxides (shown in XRD, TEM results). The CuO-based catalysts (Fig. 6b) showed a broad d–d band in the visible region [36]. This band shifted from 672 to 744 nm with a change in the supports (C_2Z_8, C_5Z_5, and C_8Z_2, respectively), indicating the coordination environment of copper species was influenced by support structures. Ratnasamy et al. [36] also observed the shift from 780 (Cu^{2+} in sixfold coordination) to 680 nm (Cu^{2+} in fourfold coordination) with changing the support from ZrO_2 to CeO_2–ZrO_2 to CeO_2.

The EPR spectra of $Ce_xZr_{1-x}O_2$ are presented in Fig. 7a. The C_8Z_2 spectra show a line at $g_{\parallel} = 1.961$ and $g_{\perp} = 1.943$, which has been assigned previously to Ce^{3+} ions [36]. It also exhibits a strong resonance line at $g_{\parallel} = 2.031$ and $g_{\perp} = 2.020$, which is attributed to O_2^- species bound to Ce^{4+} ions [29b]. The additional signal corresponds to $g = 2.047$. Since Zr^{4+} cations do not contribute to EPR, this line is probably due to the presence of Ce^{3+} ions and oxygen vacancies. Such vacancies may trap electrons that give rise to paramagnetic signal, in contrast to vacancies originated from mere relocation of O^{2-} ions into the octahedral interstitial sites [14a]. The C_5Z_5 and C_2Z_8 samples display the similar resonance line, the fine structure of which is a little poorly resolved. After the impregnation of copper species, at least two types of paramagnetic copper can be identified in the EPR spectrum (Fig. 7b). No trace of either Ce^{3+} or superoxide ions (O_2^-) is detected except fresh 06Cu/C_8Z_2. Above all, the resonance line intensities of the three fresh 06Cu/$Ce_xZr_{1-x}O_2$ samples correspondingly decrease after calcination. This result indicates that heat treatment reduces the concentration of Cu^{2+} ions in the system, probably due to the electron interaction

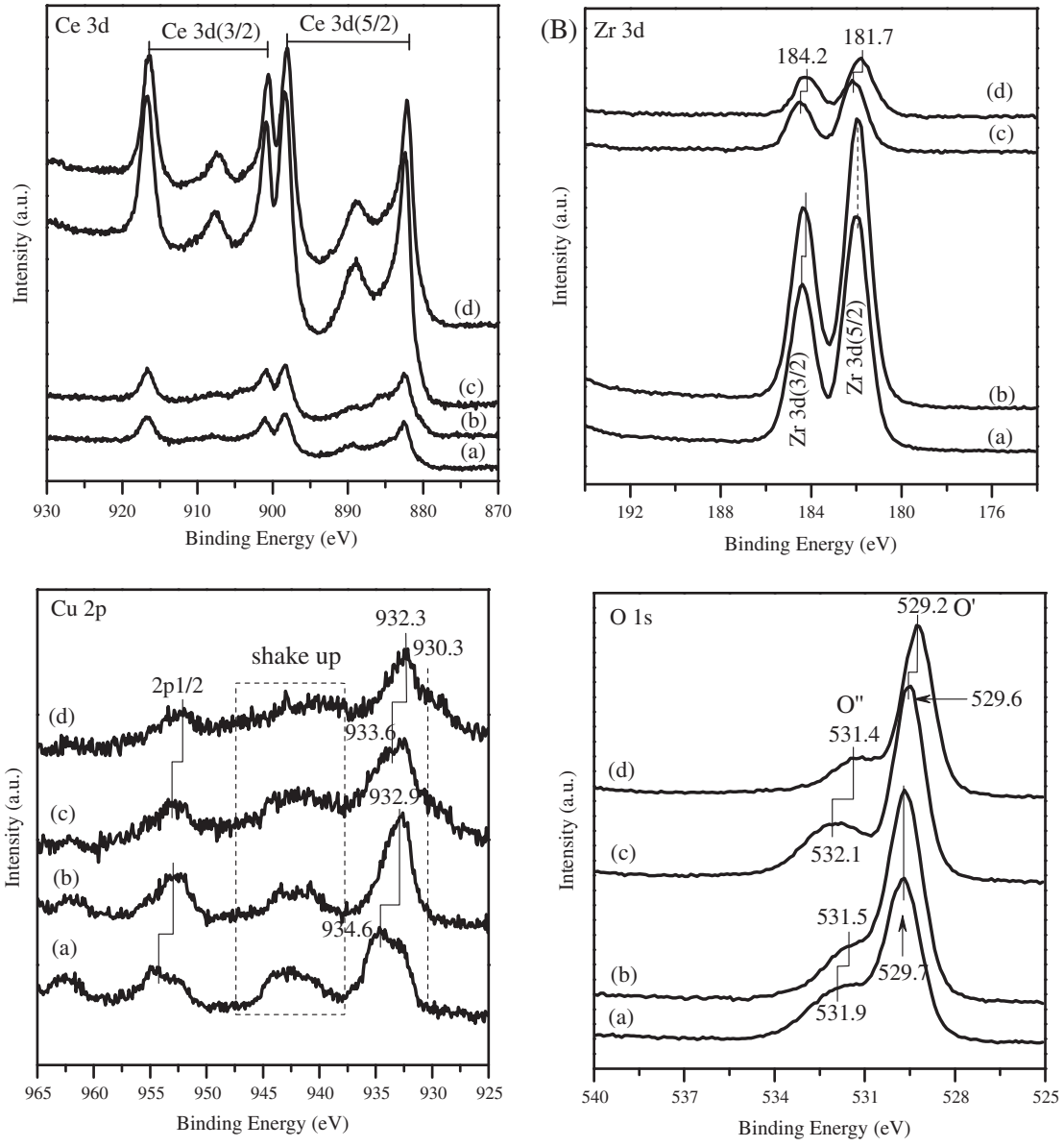

Fig. 10. XPS spectra (Ce 3d, Zr 3d, Cu 2p, O 1s) of these 03Cu/C_2Z_8 (a and b) and 03Cu/C_8Z_2 (c and d) catalysts dried at 100 °C and calcined at 450 °C, respectively.

between Cu^{2+} and Ce^{3+} ions ($Cu^{2+} + Ce^{3+} \rightarrow Cu^{+} + Ce^{4+}$). A comparison of spin Hamiltonian parameters of $06Cu/Ce_xZr_{1-x}O_2$ (Table 2) shows that these $g_{\|}$, $g_{\perp}$ and $A_{\|}$(Cu) values are different before and after calcination. The EPR parameter values of the calcined samples are also characteristic of isolated Cu^{2+} ions located in the tetragonally distorted octahedral sites [31,37]. This accounts for that the original copper species, which are distributed on the top of surface, now possibly diffuse and insert into the surface lattice by occupying the vacant sites on the (1 1 1) surface of supports. On the other hand, the isolated Cu^{2+} in the aged $06Cu/C_2Z_8$ and $06Cu/C_8Z_2$ are different in their $g_{\|}$, $g_{\perp}$ and $A_{\|}$(Cu) (former: $g_{\|} = 2.329$, $g_{\perp} = 2.044$, and $A_{\|}(Cu) = 140$ G; latter: $g_{\|} = 2.335$, $g_{\perp} = 2.038$, and $A_{\|}(Cu) = 132$ G). The species characterized by a broad isotropic signal are attributed to dipolar, interacting Cu^{2+} ions, which are centered at average $g = 2.122$, 2.106, 2.110 in $06Cu/C_2Z_8$, $06Cu/C_5Z_5$ and $06Cu/C_8Z_2$, respectively. Therefore, the types and coordination environments are influenced by the crystal structure of ceria–zirconia [36].

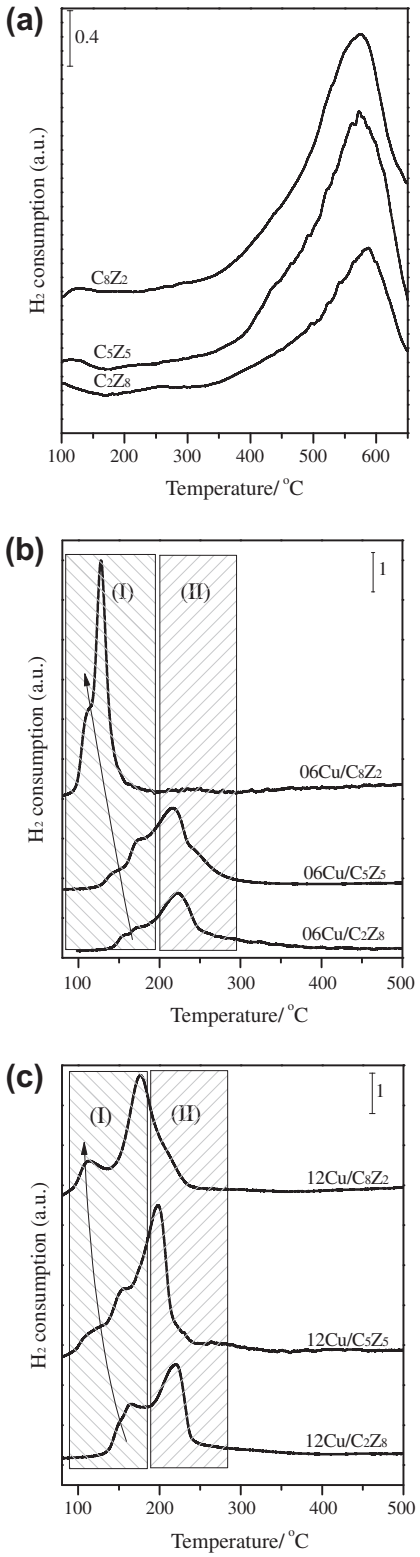

Fig. 11. H_2-TPR profiles of (a) $Ce_xZr_{1-x}O_2$, (b) $06Cu/Ce_xZr_{1-x}O_2$, and (c) $12Cu/Ce_xZr_{1-x}O_2$ catalysts.

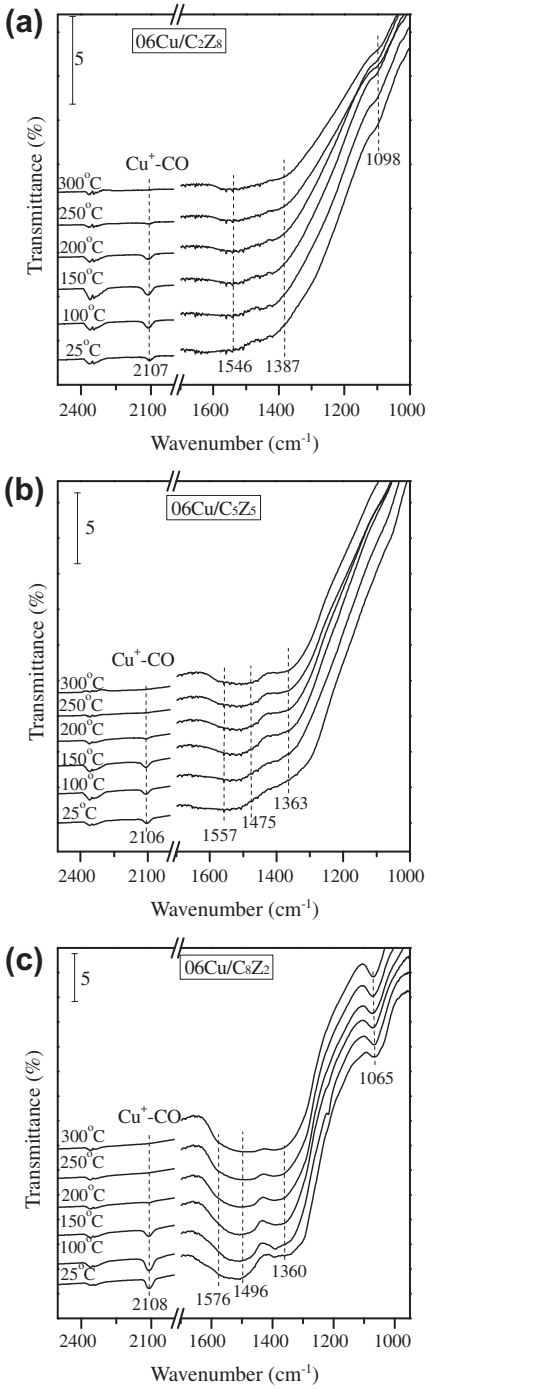

Fig. 12. In situ FTIR spectra of CO interaction with $06Cu/Ce_xZr_{1-x}O_2$ catalysts from 25 to 325 °C (a) $06Cu/C_2Z_8$, (b) $06Cu/C_5Z_5$, and (c) $06Cu/C_8Z_2$.

3.2.2. XPS analysis

The catalyst systems were analyzed by XPS to verify surface composition and elementary oxidation states. The complex spectrum of Ce 3d was decomposed into eight components with the assignment defined in Fig. 8. The chemical valence of cerium on the surface of $Ce_xZr_{1-x}O_2$ was mainly in a +4 oxidation state, and a small quantity of Ce^{3+} (v', u') co-existed [10,13,17]. Nagai et al. [8] concluded the enhancement of homogeneity of the Ce and Zr atoms could ease the valence change of the Ce ($Ce^{4+} \rightarrow Ce^{3+}$). Therefore, the presence of Ce^{3+} was partly attributed to the relative homogeneous $Ce_xZr_{1-x}O_2$ (seen in Fig. S3, XRD patterns and Raman spectra of the three samples calcined at 750 °C for 5 h did not exhibit extra peaks, indicating no phase segregation occurred [11,12a]). Another reason was probably the substitution of Ce^{4+} by Zr^{4+} ions. The spontaneous transformation of Ce^{4+} (r^{4+}_{Ce} = 0.97 Å) ion to the larger Ce^{3+} (r^{3+}_{Ce} = 1.10 Å) can compensate for this lattice contraction. Nevertheless, the part photoreduction of ceria cannot be ignored. The relative intensities of v' and u' to the other six bands increased from 16.6% to 17.2% to 22.4% with the increase in zirconium content. This revealed that the surface ratio of Ce^{3+} to Ce^{4+} on the three samples was enhanced by the incorporation of zirconia. The Zr $3d_{3/2}$ (183.7 eV) and Zr $3d_{5/2}$ (181.5 eV) peak areas and amplitudes decreased as a function of reducing zirconium content. Interestingly, the BE of the latter was higher than that in Zr metal (180.0 eV), lower than that in ZrO_2 (182.9 eV), but similar to that in ZrO_x ($0 < x < 2$, 181.4 eV) [44]. Hence, the XPS study also proved the displacement of Zr^{4+} ions into the ceria lattice. Furthermore, all the cerium to zirconium atomic ratios were a little higher than the nominal ratios calculated from the bulk composition, as indicated by the values in parentheses (Table 3), which suggested that a spot of cerium was enriched on the surface [14].

Concerning the Cu 2p spectra, it was apparent that most Cu initially present in these samples was in a +2 oxidation state and small amount in a +1 oxidation state, located at 933.2 and 930.8 eV respectively [34]. The generation of Cu^+ together with observation of Ce^{3+} species was indicative of the redox equilibrium ($Cu^{2+} + Ce^{3+} \leftrightarrow Cu^+ + Ce^{4+}$) shifting to right in these samples, which was claimed to be the source of a synergistic effect on catalytic properties [45]. This confirmed the earlier deduction from EPR. Moreover, the main peak of Cu $2p_{3/2}$ over $06Cu/C_8Z_2$ sample was broad, whereas over $06Cu/C_2Z_8$ was relatively sharp. This resulted from the stronger interaction between copper species and ceria-rich support than zirconia-rich support. Table 3 also showed that the surface Cu/Ce + Zr atomic ratios over the three catalysts appeared to be in the same level, and nearly three times the value of the nominal ratio (0.05). In this case, copper species with low loading appeared to segregate on the surface of ceria–zirconia, and the formation of a $CuCeZrO_x$ bulk solid solution did not take place.

The high-resolution spectrum for the O 1s ionization features was numerically fitted with the Gaussian features representing the primary O 1s ionization feature and chemically shifted O 1s features from chemisorbed surface species. The strong band O′ (529.9 eV) was attributed to characteristic oxygen of the metal oxides [32], while the shoulder O″ with higher binding energy (532.1 eV) was the result of chemisorbed oxygen [12]. Although no chemical shift was found in the O 1s feature with changing the oxide composition, the O/(Cu + Ce + Zr) atomic ratios (Table 3) exceptionally increased with the increase in zirconium. This should be due to the presence of Ce^{3+} over ceria-rich sample that favored the formation of oxygen vacancy in the oxide surface. In addition, the O/(Cu + Ce + Zr) ratios over $06Cu/C_2Z_8$ and $06Cu/C_5Z_5$ were higher than the nominal ratio (1.95) of the fully oxidized surface, but over $06Cu/C_8Z_2$ were lower. The excess surface oxygen was attributed to the high concentration of surface oxygen as an adsorbed layer of CO_2, CO or water [13].

In order to substantiate XRD results and further understand the difference of copper dispersion, XPS is performed on yCu/C_2Z_8 and yCu/C_8Z_2 catalysts with a series of amounts (seen in Fig. S4). The XPS peak intensity ratio $I_{Cu}/I_{(Ce+Zr)}$ is linear fitted as a function of copper loading amount. As represented in Fig. 9a and b, the dispersion capacity of copper oxide on zirconia-rich and ceria-rich phases is 0.46 and 0.73 mmol/100 m^2 $Ce_xZr_{1-x}O_2$, respectively. Remarkably, ceria-rich phase can disperse copper species more effectively than zirconia-rich phase. This is consistent with the XRD quantitative results.

XPS was further performed on the fresh and calcined $03Cu/C_2Z_8$ and $03Cu/C_8Z_2$, which provided information about the surface interaction and the chemical state of elements in the near-surface region. As present in Fig. 10A and B, in comparison with zirconia-rich phase catalyst before and after calcination (a and b), the valence of cerium was predominant in a 4+, and no obvious chemical shift took place on Ce 3d. However, the intensity of v' and u' peaks for Ce^{3+} increased, and the Zr $3d_{3/2}$ slightly shifted to low binding energy. For ceria-rich phase catalyst (c and d), calcination at 450 °C resulted in the chemical shift of Ce 3d and Zr 3d peaks, and the decrease in peak intensity. These differences indicated that the metals' environments were different near the cerium or zirconium sites, which may be due to the electronic state interaction between ceria–zirconia and the introduced species in the catalysts [12b].

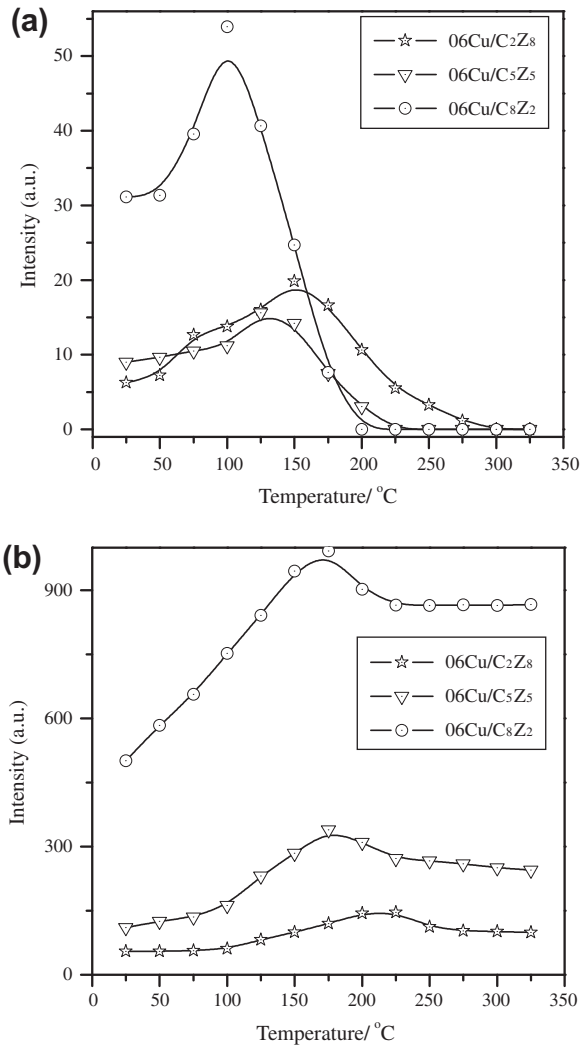

Fig. 13. Integrated intensity of IR spectra for (a) copper carbonyls and (b) carbonates over $06Cu/Ce_xZr_{1-x}O_2$ catalysts as a function of temperature.

As shown in Fig. 10C, calcination led to not only the chemical shift of Cu $2p_{3/2}$ and $2p_{1/2}$ signals to low binding energy but also the decrease in shake-up peak due to the characteristic Cu^{2+}. Moreover, a shoulder at 930.3 eV appeared in ceria-rich catalyst, which was assigned to the reduced state of copper species [12b]. The surface Cu/(Cu + Ce + Zr) atomic ratios decreased from 0.08 to 0.06 and 0.12 to 0.09 for zirconia-rich and ceria-rich catalysts, respectively. Generally, the coordination geometry of Cu^{2+} ions can be studied by determining the intensity ratios of the satellite to the corresponding principal peak (I_{sat}/I_{pp}). The ratio of I_{sat}/I_{pp} decreases as the number of oxygen ions coordinated with Cu^{2+} ions increases [[42b] and therein]. When compared with the I_{sat}/I_{pp} values of fresh $03Cu/C_2Z_8$ and $03Cu/C_8Z_2$, after calcination they increase from 0.35 to 0.37 and from 0.51 to 0.59, respectively. Therefore, the local electron property and the coordination environment of dispersed copper species are greatly modified after calcination, probably due to an interfacial interaction between copper and the underlying supports, which resulted in the insertion of copper from the surface into lattice. In addition, the I_{sat}/I_{pp} ratios were distinguishable in zirconia-rich (0.37) and ceria-rich (0.59) phases, which were all different from the characteristic value for pure Cu^{2+} (0.55) [12b]. This indicated that the coordination environment of cupric ions on ceria-rich phase was close to octahedral symmetry, whereas on zirconia-rich phase was distorted. This coincided with EPR analysis.

Regarding the O 1s spectra (Fig. 10D), the O″ at higher energies, attributed to adsorbed hydroxyl, moved from 531.9 to 531.4 and from 532.1 to 531.5 eV on $03Cu/C_2Z_8$ and $03Cu/C_8Z_2$, respectively. However, the shift of O′ at 529–530 eV, due to the lattice oxygen bound to metal ions, just happened on ceria-rich catalyst. Interestingly, the surface O/(Cu + Ce + Zr) atomic ratios of $03Cu/C_2Z_8$ and $03Cu/C_8Z_2$ after calcination decreased from initial 2.06 to 1.99 and 2.55 to 2.29. Other than this, the proportion of O″/(O″ + O′) correspondingly decreased from 32.9% to 29.1% and from 34.0% to 27.5%. The increase in the concentration of lattice oxygen replied the incorporation of copper into the lattice with the capping oxygen.

3.3. Reduction properties of $CuO/Ce_xZr_{1-x}O_2$ catalysts (H_2-TPR, CO-IR)

Fig. 11 compared the H_2-TPR results of these samples. The pure ceria–zirconia supports started the reduction of surface oxygen [15,16] from 150 °C and showed the maximum at 560 °C (Fig. 11a). For the catalysts with low copper loading (Fig. 11b), at least two reduction peaks were observed in low-temperature range. These intensive peaks were associated with the concurrent reduction of different types of copper species and $Ce_xZr_{1-x}O_2$ surface oxygen [32]. The H_2 consumption, which was higher than that expected for complete reduction of Cu^{2+} to Cu^0 (Fig. S5), could prove this viewpoint. The reduction of $Ce_xZr_{1-x}O_2$ supports was

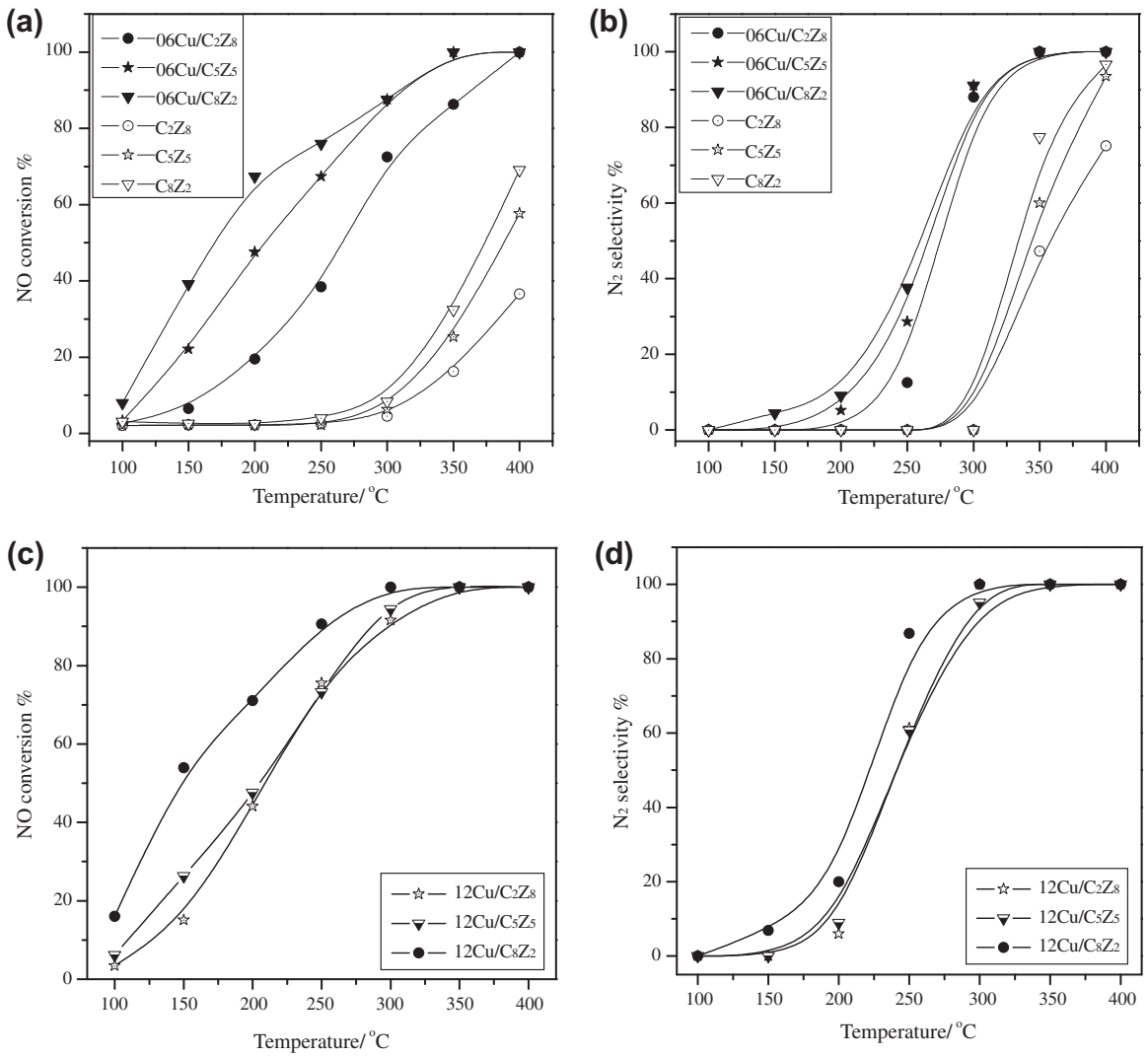

Fig. 14. NO conversion (%) and N_2 selectivity (%) of supports and $CuO/Ce_xZr_{1-x}O_2$ catalysts as a function of temperature.

due to the promotion by hydrogen spill from the reduced copper entity to its surface [33]. In the zone (I), two peaks were proposed as the reduction of the dispersed copper species strongly interacting with ceria, whereas in the zone (II) as copper oxide in proximity to zirconia and the less dispersed one. Obviously, an effect of the support composition on the TPR profiles can be discerned. A moderate shift of the reduction peaks to low temperatures took place with the increase in cerium content, and no reduction peak was found in the zone (II) of $06Cu/C_8Z_2$, probably because it disperses well. Similar information was also obtained from the samples with high copper loading (Fig. 11c). These reduction peaks in the zone (II) were considered partially from the contribution of crystalline CuO [38]. These assignments were in accordance with the above XRD, Raman, UV–vis and XPS results. From the H_2-TPR profiles, it was reasonably imagined that copper species seemed to preferentially interact with ceria, and the pseudocubic (t'') structure could promote the reduction of the resultant catalyst more easily than the tetragonal (t) did. The stronger interaction between copper species and ceria-rich support could account for this behavior.

To further gain insight into the reduction property of the catalysts, in situ FTIR of CO as a probe molecule interacting with $06Cu/Ce_xZr_{1-x}O_2$ was measured in a TPR procedure. As shown in Fig. 12, exposure of $06Cu/Ce_xZr_{1-x}O_2$ to CO at room temperature gave IR bands at about 2107 cm^{-1} due to the adsorption of CO on Cu^+ ions [45]. Similar IR spectra assignable to chemisorbed carbonates (1065–1098, 1360–1390, 1470–1499 cm^{-1} and 1540–1580 cm^{-1} for polydentate and bidentate, respectively [18,29,30,45]) were clearly seen over $06Cu/C_2Z_8$, $06Cu/C_5Z_5$ and $06Cu/C_8Z_2$, which were very stable even after heat treatment up to 300 °C. Important information was the evolution of the copper carbonyl intensity with temperature during the CO-TPR runs. As shown in Fig. 13a, Cu^+–CO on $06Cu/C_2Z_8$ showed the maximum intensity at 150 °C and completely disappeared at 300 °C. The increase and disappearance of copper carbonyl suggested that the progressive reduction of Cu^{2+} to Cu^+ was favored up to that temperature, while reduction of Cu^+ to metallic copper would happen at higher temperature. In turn, reduction of Cu^{2+} to Cu^+ on $06Cu/C_5Z_5$ would be produced up to 125 °C and subsequent reduction to metallic copper would occur above this temperature. The above behaviors on $06Cu/C_8Z_2$ were favored at 100 °C. This analysis was in agreement with the reports about CuCeTb catalysts [46]. Correspondingly, the intensity of carbonates (Fig. 13b) increased in parallel from 25 to 200 °C and kept consistent at high temperatures. These differences accounted for that the stability of Cu^+-carbonyl was affected by the support composition. The ceria-rich phase had the greater ability to assist the copper oxide in changing the chemical valence (Cu^{2+} to Cu^+/Cu^0) and support in supplying surface oxygen (the formation of oxygen vacancies) at low temperatures, but difficult for the zirconia-rich phase.

3.4. Relationship of structure with catalytic activity

Fig. 14 showed the NO conversion and N_2 selectivity as a function of temperature for NO + CO reaction over pure $Ce_xZr_{1-x}O_2$ and $Cu/Ce_xZr_{1-x}O_2$ catalysts. At low temperatures (≤300 °C), the NO conversion and N_2 selectivity over the supports (Fig. 14a and b) were identical (close to 0%). While at high temperatures (≥350 °C), the values were dependent on the compositions. C_8Z_2 showed the higher activity and N_2 selectivity than C_5Z_5 and C_2Z_8 did, although its surface area was lowest among them. This was possibly due to the formation of more oxygen vacancies in C_8Z_2 [39,47]. After the impregnation of copper species with low loading (Fig. 14a and b), however, these catalysts exhibited the different activity and selectivity blow 300 °C following the order of $06Cu/C_8Z_2 > 06Cu/C_5Z_5 > 06Cu/C_2Z_8$, but no difference could be found over $06Cu/C_8Z_2$ and $06Cu/C_5Z_5$ above 300 °C. For the samples with high loading (Fig. 14c and d), the order was ranked as $12Cu/C_8Z_2 > 12Cu/C_5Z_5 \approx 12Cu/C_2Z_8$ below 350 °C. We also compared the TOF of NO over per copper atom, as shown in Fig. 15. In the temperature range 100–250 °C, $06Cu/C_8Z_2$ obviously showed the highest value, followed by $06Cu/C_5Z_5$ and $06Cu/C_2Z_8$ in sequence. On the other hand, $12Cu/C_8Z_2$ showed a TOF of 0.34 s^{-1} at 180 °C, which was lower than that on $06Cu/C_8Z_2$ (0.81 s^{-1} at 180 °C). Therefore, the crystalline copper oxide appeared not to contribute

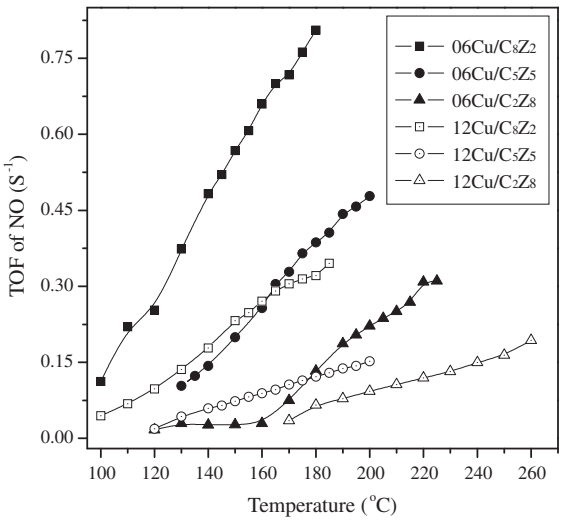

Fig. 15. Turnover frequencies (TOF, s^{-1}) of NO over per copper atom in these CuO/$Ce_xZr_{1-x}O_2$ catalysts as a function of temperature.

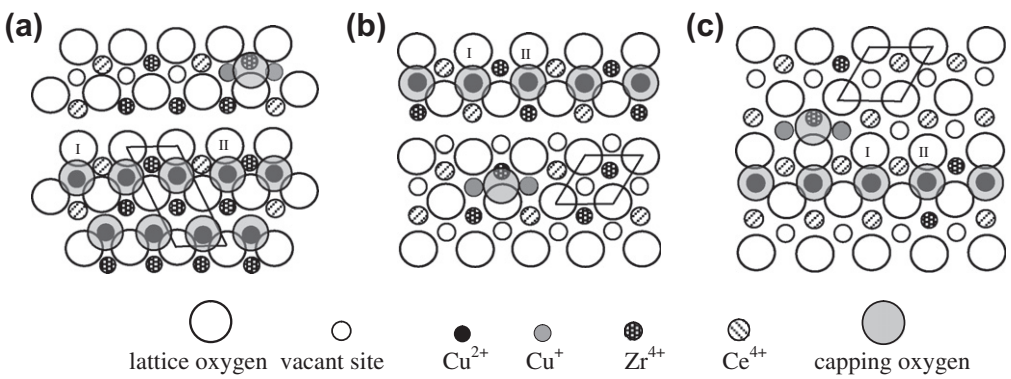

Fig. 16. The diagram of Cu^{2+} and Cu^+ incorporated in the vacant sites on the (1 1 1) plane of the $Ce_xZr_{1-x}O_2$ supports (a) $Ce_{0.2}Zr_{0.8}O_2$, (b) $Ce_{0.5}Zr_{0.5}O_2$, and (c) $Ce_{0.8}Zr_{0.2}O_2$.

to NO conversion. Since all these catalysts have the similar particle size in the nanoscale, the nanosize effect can be ruled out. Secondly, the surface area of supports and the loading amounts of copper species were not the main factors influencing the activity. Consequently, these unusual results at low temperatures were originated from the differently synergistic interaction between copper and $Ce_xZr_{1-x}O_2$ supports. When trying to understand and interpret the measured catalytic data from the viewpoint of interaction, two central questions evolved:

I. What caused the observed differences in the synergetic interaction between copper species and $Ce_xZr_{1-x}O_2$ phases?
II. Why was copper oxide more active on ceria-rich than on zirconia-rich phase?

When addressing the first question, we imagined that the surface structure of $Ce_xZr_{1-x}O_2$ supports would be an essential reason. It is generally accepted that tetragonal ZrO_2 represents a slightly distorted CaF_2 type structure [43], while CeO_2 possesses a typical fluorite structure. Alternatively, it can be described as an array of cations forming the face-centered cubic lattice with oxygen ions occupying the tetrahedral interstitial sites [14b]. The octahedral sites in a perfect fluorite structure are empty, which are considered to locate in the exposed (1 1 1) surface. The crystal structure of tetragonal and pseudocubic $Ce_xZr_{1-x}O_2$ are similar to pure t-ZrO_2 and CeO_2, thus being proposed to have the similar vacant sites on the (1 1 1) plane. Noticeably, their ionic radius, lattice parameters and compositions (Ce/Zr ratios) determined the different atom arrangement on this surface. According to our previous incorporation model [42,43], it was presumed that tetragonal vacant sites existed on the C_2Z_8 (1 1 1) surface, cubic vacant sites on the C_8Z_2, and the mixed on the C_5Z_5. In this case, how were the copper species stabilized? As discussed in Sections 3.1 and 3.2 about structural and surface characteristics, when at low loadings, copper ions could be incorporated into the surface lattice by occupying the vacant site on the (1 1 1) plane. The capping oxygen was accompanied for charge compensation, as shown in Fig. 16. As a result, the incorporation led to the generation of synergetic interaction between copper and ceria–zirconia (1 1 1) surface. Liu et al. [49] also proposed that the copper ions at the interfacial region of the finely dispersed CuO clusters and CeO_2 could penetrate into the cerium oxide lattice by occupying the vacant sites of the cerium ions on the (0 0 1) plane. For zirconia-rich sample, Cu^{2+} ions were probably located as the elongated and compressed coordination with the C_{3v} or trigonal bipyramid symmetry. For ceria-rich sample, Cu^{2+} ions at the interfacial area can penetrate into the cubic vacant sites to form an unstable five-coordination structure and can associate with the adjacent cerium ions to generate the electronic interaction. The sites geometry of copper species was consequently dissimilar. As reported elsewhere [[2] and therein], lattice strain can reflect surface effects (differences in local symmetry and distances with respect to the bulk). Hence, we imagined that there should be some connection between the structure stability and lattice strain of these studied catalysts. It was proposed that the above coordination structure of ceria-rich catalyst with the high strain would be less stable, while that of zirconia-rich catalyst with the low strain would be stable. Therefore, this information explained why there was a stronger synergetic interaction between copper- and ceria-rich phase than zirconia-rich phase.

According to the reports [25,48], these easily reduced Pt/$CeZrO_2$ catalyst showed the higher activity for NO + CO reaction, which was pronounced as a structure-sensitive reaction. Moreover, the redox-type mechanism between Cu^{2+} and Cu^0 was promising for the simple NO + CO reaction over the supported copper species [50]. Along this line, addressing the second question, we suggested that when compared with the zirconia-rich surface, the stronger interaction between the incorporated copper species and the ceria-rich surface could bring down the reduction temperature of Cu^{2+} ions and support surface oxygen. The facility for achieving partial reduction of copper oxide entities at the interface zone, which was favored by an increase in dispersion of copper component, may be most significant in accounting for the different activities. In the second place, the quick change of copper valence in ceria-rich catalyst and strong electron state interaction also greatly contributed to the higher activity. The EPR, XPS, H_2-TPR and CO-IR results could support these ideas. Hence, the reaction pathway of NO transformation into N_2 and N_2O essentially depended on the

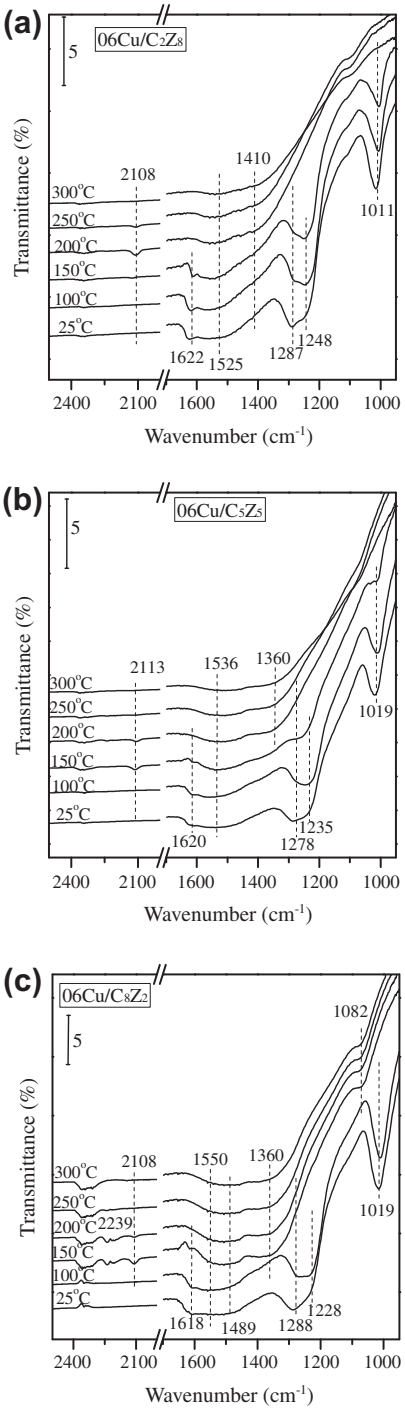

Fig. 17. In situ FTIR spectra of CO and NO co-interaction with 06Cu/$Ce_xZr_{1-x}O_2$ catalysts at different temperatures (a) 06Cu/C_2Z_8, (b) 06Cu/C_5Z_5, and (c) 06Cu/C_8Z_2.

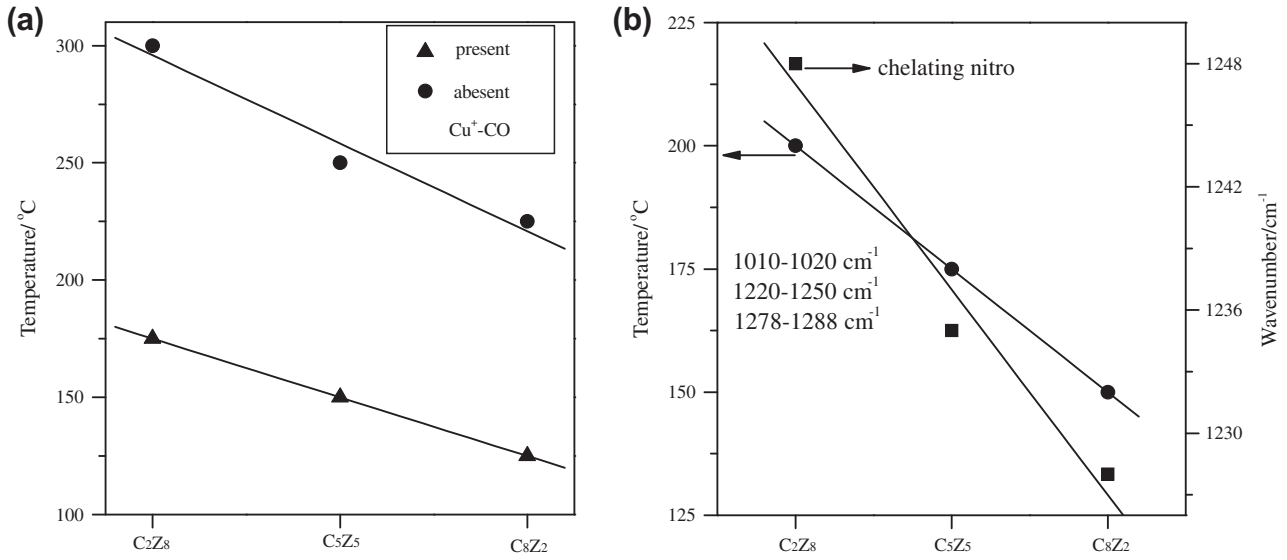

Fig. 18. (a) The temperature for the presence and absence of Cu^+–CO over these three catalysts; (b) the reaction temperature of adsorbed NO and wave number of chelating nitro over these three catalysts.

characteristics of the synergistic interaction between copper species and ceria–zirconia supports.

3.5. NO and CO co-interaction with $CuO/Ce_xZr_{1-x}O_2$ catalysts

In situ FTIR for NO and CO co-interaction with $CuO/Ce_xZr_{1-x}O_2$ was performed to further probe the surface species and the correlation of structure–activity over these catalysts. As shown in Fig. 17, NO molecules appeared to preferentially interact with these catalysts at room temperature, thus very intensive bands for four differently coordinated NOx species in the region 1000–1700 cm^{-1} now dominated the spectra. An increase in temperature up to 200 °C led to a decrease and disappearance, respectively, of chelating nitro (1220–1250 cm^{-1}) [40], monodentate (1275–1290, 1470–1510 cm^{-1}) [20,21] and bridge nitrates (1010–1020/1610–1620 cm^{-1}) [23,41], and to the progressive accumulation of bidentate nitrates and carbonates (1360, 1480–1570 cm^{-1}, formed by the adsorption of CO_2) [27,28]. Further increasing the temperature to 300 °C resulted in the decrease in the residual bands (1360, 1480–1540 cm^{-1}). Concerning the spectral features in the region of 2000–2500 cm^{-1}, one can distinguish bands at ca. 2116, 2220–2240 and 2360 cm^{-1} for Cu^+–CO, N_2O [28] and CO_2, respectively. These results indicated that reaction of the adsorbed NO species with CO had readily taken place rather than their rearrangement or desorption (seen in Fig. S6, the adsorbed NO species were stable up to 300 °C during the TPD process). The formation of N_2O should not be originated from the decomposition of adsorbed nitrates, because N_2O was not detected during the IR-TPD process (data not shown). In addition, Cu^+–CO and N_2O over these samples totally vanished when reaching 300 °C, which might be due to either no production of N_2O or its reaction with CO at high temperature. This was in accordance with our activity test results (low N_2 selectivity at low temperature and high at above 250 °C). This was related to its reaction mechanism over copper-based catalysts. The NO reduction by CO was believed to proceed in two steps, first partial reduction of NO to N_2O and then subsequent reduction of N_2O to N_2 [[48] and therein].

More important to this system was the results obtained upon the comparison of the stability of copper carbonyl and adsorbed NO species. In Fig. 18a, the temperatures for the presence/absence of Cu^+–CO were in the order of $C_2Z_8 > C_5Z_5 > C_8Z_2$, which suggested that the ceria-rich phase had the greater ability to accelerate the CO desorption or/and rapid change in valence states of copper than zirconia-rich did during the reaction process. According to the report [48], Cu^{2+} ions acted as NO adsorption sites, while Cu^+ ions acted as recipients of the O atoms produced through the dissociation. Therefore, it ensured an inhibition of the reduction of NO by increased CO partial pressures, due to the adsorption of CO on these sites. It was presumed that the easy desorption of CO was beneficial for the enhancement of activity. So, our above suggestion could explain why the higher activity was obtained over the ceria-rich phase sample in the present reaction system (CO:NO = 2:1). This information further confirmed our above consideration (Section 3.4). The rapid change in valence state of copper species was a crucial part of this reaction mechanism. Apart from the above discussion, it was found that the adsorbed bridge, monodentate nitrates and chelating nitro over these samples, positioned at 1010–1020, 1278–1288 and 1220–1250 cm^{-1}, respectively, completely disappeared with the decrease in temperature as C_2Z_8, C_5Z_5, C_8Z_2 in sequence (Fig. 18b). Furthermore, the wave number of chelating nitro also red shifted from 1248 to 1228 cm^{-1} in turn, suggesting the interaction of NO with Cu/C_8Z_2 was strengthened, thus the N–O bond was weakened. These findings demonstrated that the adsorbed NO species over zirconia-rich (t) catalyst were stable, whereas over ceria-rich (t'') catalyst were less stable due to its superior redox activity.

4. Conclusions

This work studied the correlation of structural characteristics with catalytic performance of $CuO/Ce_xZr_{1-x}O_2$ (x = 0.2, 0.5, 0.8) catalysts for NO reduction by CO. Combined with XRD, Raman, HR-TEM, UV–vis, EPR and XPS results, it was demonstrated that (1) the dispersion capacity of CuO on the $Ce_xZr_{1-x}O_2$ was influenced by the crystal structures of supports, and the ceria-rich (pseudocubic t'') phase could anchor and stabilize the copper species more effectively than the zirconia-rich (t) phase. (2) The copper species could penetrate into the surface lattice by occupying the vacant sites on the predominantly exposed (1 1 1) surface of ceria–zirconia, and their interaction with ceria-rich phase was much stronger than that with zirconia-rich phase. (3) The differences in the coordination environments and lattice strains of $CuO/Ce_xZr_{1-x}O_2$ were

considered as a reason for the different synergistic interaction between them. H_2-TPR and CO-IR results suggested that compared with the zirconia-rich phase, the ceria-rich phase had the greater ability to facilitate the reduction of copper species and support surface oxygen layer, which might be due to its unstable five-coordination structure. In situ FTIR results revealed that the synergistic effect between copper and t'' phase could easily promote the desorption of copper carbonyl and the activation of adsorbed NO (bridge nitrate, chelating nitro) species, whereas difficultly for t phase. Therefore, $CuO/Ce_{0.8}Zr_{0.2}O_2$ showed the higher activity toward NO reduction than $CuO/Ce_{0.5}Zr_{0.5}O_2$ and $CuO/Ce_{0.2}Zr_{0.8}O_2$.

Acknowledgments

The financial supports of the National Natural Science Foundation of China (Nos. 20873060 and 20973091), the Project of Jiangsu Innovation Talent (BK2008001), Jiangsu Scientific Research Foundation for Graduate (CX09B-003Z) and Scientific Research Foundation of Graduate School of Nanjing University are gratefully acknowledged.

Appendix A. Supplementary material

Supplementary data associated with this article can be found, in the online version, at doi:10.1016/j.jcat.2010.07.024.

References

[1] M. Yashima, J. Phys. Chem. C 113 (2009) 12658.
[2] J.A. Rodriguez, X. Wang, G. Liu, J.C. Hanson, J. Hrbek, C.H.F. Peden, A. Iglesias-Juez, M. Fernández-Garc, J. Mol. Catal. A: Chem. 228 (2005) 11.
[3] V.S. Escribano, E.F. López, M. Panizza, C. Resini, J.M.G. Amores, G. Busca, Solid State Sci. 5 (2003) 1369.
[4] R.D. Monte, J. Kašpar, J. Mater. Chem. 15 (2005) 633.
[5] F. Zhang, C.H. Chen, J. Am. Ceram. Soc. 89 (2006) 1028.
[6] B.M. Reddy, P. Lakshmanan, A. Khan, J. Phys. Chem. B 109 (2005) 13545.
[7] M.P. Yeste, J.C. Hernández, S. Trasobares, S. Bernal, G. Blanco, J.J. Calvino, J.A. Pérez-Omil, J.M. Pintado, Chem. Mater. 20 (2008) 5107.
[8] Y. Nagai, T. Yamamoto, T. Tanaka, S. Yoshida, T. Nonakaa, T. Okamotoa, A. Suda, M. Sugiura, Catal. Today 74 (2002) 225.
[9] S. Letichevsky, C.A. Tellez, R.R. de Avillez, M.I.P. da Silva, M.A. Fraga, L.G. Appel, Appl. Catal. B: Environ. 58 (2005) 203.
[10] M. Alifanti, B. Baps, N. Blangenois, J. Naud, P. Grange, B. Delmon, Chem. Mater. 15 (2003) 395.
[11] R.O. Fuentes, R.T. Baker, J. Phys. Chem. C 113 (2009) 914.
[12] (a) B.M. Reddy, P. Bharali, P. Saikia, J. Phys. Chem. C 112 (2008) 11729;
(b) B.M. Reddy, K.N. Rao, P. Bharali, Ind. Eng. Chem. Res. 48 (2009) 8478.
[13] A.E. Nelson, K.H. Schulz, Appl. Surf. Sci. 210 (2003) 206.
[14] (a) E. Mamontov, T. Egami, J. Phys. Chem. B 104 (2000) 11110;
(b) E. Mamontov, R. Brezny, M. Koranne, T. Egami, J. Phys. Chem. B 107 (2003) 13007.
[15] F. Fally, V. Perrichon, H. Vidal, J. Kaspar, G. Blanco, J.M. Pintado, S. Bernal, G. Colon, M. Daturi, J.C. Lavalley, Catal. Today 59 (2000) 373.
[16] J. Ouyang, H.M. Yang, J. Phys. Chem. C 113 (2009) 6921.
[17] R. Si, Y.W. Zhang, S.J. Li, B.X. Lin, C.H. Yan, J. Phys. Chem. B 108 (2004) 12481.
[18] M. Daturi, C. Binet, J.C. Lavalley, G. Blanchard, Surf. Interf. Anal. 30 (2000) 273.
[19] E. Finocchio1, M. Daturia, C. Bineta, J.C. Lavalleya, G. Blanchard, Catal. Today 52 (1999) 53.
[20] B. Azambre, L. Zenboury, A. Koch, J.V. Weber, J. Phys. Chem. C 113 (2009) 13287.
[21] A. Adamski, E. Tabor, B. Gil, Z. Sojka, Catal. Today 119 (2007) 114.
[22] M. Boaro, C. de Leitenburg, G. Dolcetti, A. Trovarelli, J. Catal. 193 (2000) 338.
[23] I. Atribak, B. Azambre, A.B. L? pez, A. García-García, Appl. Catal. B: Environ. 92 (2009) 126.
[24] M. Adamowska, S. Muller, P. Da Costa, A. Krzton, P. Burg, Appl. Catal. B: Environ. 74 (2007) 278.
[25] H.O. Zhu, J.R. Kim, S.K. Ihm, Appl. Catal. B: Environ. 86 (2009) 87.
[26] M. Haneda, K. Shinoda, A. Nagane, O. Houshito, H. Takagi, Y. Nakahara, K. Hiroe, T. Fujitani, H. Hamada, J. Catal. 259 (2008) 223.
[27] M. Kantcheva, O. Samarskaya, L. Ilieva, G. Pantaleo, A.M. Venezia, D. Andreeva, Appl. Catal. B: Environ. 88 (2009) 113.
[28] R.D. Monte, J. Kašpar, P. Fornasiero, M. Graziani, C. Pazé, G. Gubitosa, Inorg. Chim. Acta 334 (2002) 318.
[29] (a) A.B. Hungría, A. Iglesias-Juez, A. Martínez-Arias, M. Fernández-García, J.A. Anderson, J.C. Conesa, J. Soria, J. Catal. 206 (2002) 281;
(b) A. Martínez-Arias, M. Fernández-García, A.B. Hungría, A. Iglesias-Juez, O. Gálvez, J.A. Anderson, J.C. Conesa, J. Soria, G. Munuera, J. Catal. 214 (2003) 261.
[30] L. Ilieva, G. Pantaleo, I. Ivanov, A.M. Venezia, D. Andreeva, Appl. Catal. B: Environ. 65 (2006) 101.
[31] P.G. Harrison, I.K. Ball, W. Azelee, W. Daniell, D. Goldfarb, Chem. Mater. 12 (2000) 3715.
[32] G. Avgouropoulos, T. Ioannides, Appl. Catal. B: Environ. 67 (2006) 1.
[33] M. Manzoli, R. Di Monte, F. Boccuzzi, S. Coluccia, J. Kašpar, Appl. Catal. B: Environ. 61 (2005) 192.
[34] S.P. Wang, T.Y. Zhang, Y. Su, S.R. Wang, S.M. Zhang, B.L. Zhu, S.H. Wu, Catal. Lett. 121 (2008) 70.
[35] (a) B. Skårman, L.R. Wallenberg, P.O. Larsson, A. Andersson, J.O. Bovin, S.N. Jacobsen, U. Helmersson, J. Catal. 181 (1999) 6;
(b) B. Skårman, T. Nakayama, D. Grandjean, R.E. Benfield, E. Olsson, K. Niihara, L.R. Wallenberg, Chem. Mater. 14 (2002) 3686.
[36] P. Ratnasamy, D. Srinivas, C.V.V. Satyanarayana, P. Manikandan, R.S. Senthil Kumaran, M. Sachin, V.N. Shetti, J. Catal. 221 (2004) 455.
[37] J.F. Chen, J.J. Zhu, Y.Y. Zhan, X.Y. Lin, G.H. Cai, K.M. Wei, Q. Zheng, Appl. Catal. A: Gen. 363 (2009) 208.
[38] L. Ma, M.F. Luo, S.Y. Chen, Appl. Catal. A: Gen. 242 (2003) 151.
[39] B. Wen, M.Y. He, Appl. Catal. B: Environ. 37 (2002) 75.
[40] Y.W. Chi, S.S.C. Chuang, J. Catal. 190 (2000) 75.
[41] L.J. Liu, B. Liu, L.H. Dong, J. Zhu, H.Q. Wan, K.Q. Sun, H.Y. Zhu, L. Dong, Y. Chen, Appl. Catal. B: Environ. 90 (2009) 578.
[42] (a) L. Dong, Y.H. Hu, F. Xu, D. Lu, B. Xu, Z. Hu, Y. Chen, J. Phys. Chem. B 104 (2000) 78;
(b) L. Dong, Z. Liu, Y.H. Hu, B. Xu, Y. Chen, J. Chem. Soc., Faraday Trans. 94 (1998) 3033.
[43] Z. Liu, W.J. Ji, L. Dong, Y. Chen, J. Catal. 172 (1997) 243.
[44] G. Postole, B. Chowdhury, B. Karmakar, K. Pinki, J. Banerji, A. Auroux, J. Catal. 269 (2010) 110.
[45] C.S. Polster, H. Nair, C.D. Baertsch, J. Catal. 266 (2009) 308.
[46] A. Hornés, P. Bera, A.L. Cámara, D. Gamarra, G. Munuera, A. Martínez-Arias, J. Catal. 268 (2009) 367.
[47] S. Roy, M.S. Hegde, G. Madras, Appl. Energy 86 (2009) 2283.
[48] V.I. Pârvulescu, P. Grange, B. Delmon, Catal. Today 46 (1998) 233.
[49] W. Liu, M. Flytzani-Stephanopoulos, J. Catal. 153 (1995) 317.
[50] F. Amano, S. Suzuki, T. Yamamoto, T. Tanaka, Appl. Catal. B: Environ. 64 (2006) 282.